

SiO Maser Survey of the Inner Bar of the Galactic Bulge

Takahiro FUJII,^{1,2} Shuji DEGUCHI,³ Yoshifusa ITA,^{4,5}
 Hideyuki IZUMIURA,⁶ Osamu KAMEYA,^{1,7} Atsushi MIYAZAKI,^{3,8}
 and
 Yoshikazu NAKADA^{4,9}

¹ VERA Project Office, National Astronomical Observatory, 2-21-1 Osawa, Mitaka, Tokyo 181-8588

² Faculty of Science, Kagoshima University, 1-21-35 Korimoto, Kagoshima, Kagoshima 890-0065

³ Nobeyama Radio Observatory, National Astronomical Observatory,
 Minamimaki, Minamisaku, Nagano 384-1305

⁴ Institute of Astronomy, School of Science, The University of Tokyo,
 2-21-1 Osawa, Mitaka, Tokyo 181-0015

⁵ Institute of Space and Astronautical Science, Japan Aerospace Exploration Agency,
 Yoshinodai 3-1-1, Sagamihara, Kanagawa 229-8510

⁶ Okayama Astrophysical Observatory, National Astronomical Observatory,
 Kamogata, Asakuchi, Okayama 719-0232

⁷ Mizusawa Astrodynamics Observatory, National Astronomical Observatory,
 2-12 Hoshigaoka, Mizusawa, Iwate 023-0861

⁸ Shanghai Astronomical Observatory, Chinese Academy of Sciences
 80 Nandan Road, Shanghai, 200030, P.R. China

⁹ Kiso Observatory, School of Science, The University of Tokyo,
 Mitake, Kiso, Nagano 397-0101
 (PASJ 58, No. 3 in press ; Ver 1.3 – May 1, 2006)

(Received 2005 November 24; accepted 2006 March 26)

Abstract

We surveyed 291 MSX/2MASS infrared objects in the $7^\circ \times 2^\circ$ area of the galactic center in the 43 GHz SiO $J = 1-0$ $v = 1$ and 2 maser lines, obtaining accurate radial velocities of 163 detected objects. The surveyed area is the region where the IRAS catalog is incomplete due to contamination by high source density. The objects in the present MSX/2MASS sample were chosen to have similar infrared characteristics to those of the previous SiO-maser-survey samples based on the color selected IRAS sources. The sampling based on the 2MASS catalog causes a bias to the foreside objects of the bulge due to heavy obscuration by interstellar dust; the detections are considerably leaned on the $V_{lsr} < 0$ side. The $l-v$ diagram reveals two conspicuous features, which were not present or tenuous in the previous studies: one feature indicating a linear velocity increase with longitude with $|l| < 1.5^\circ$, which is likely associated with the inner bar, and the other feature having considerably eccentric velocities more than those of the normal x_1 -orbit family feature. The extinction-corrected K magnitudes (if used as a distance modulus) tend to show a sequential deposition of these objects along the line of sight toward the Galactic center depending on their radial velocities. The tendency that appeared in the distance measures is consistent with the bulge-bar dynamical model utilizing the periodic orbit families in the bar potential.

Key words: Galaxy: center, kinematics and dynamics — masers — stars: AGB and post-AGB

1. Introduction

The Galactic bulge embraces a large number of mass-losing Asymptotic Giant Branch (AGB) stars (Habing 1987). They supply gases to the Galactic nuclear disk, gradually fueled for the activity of the Galactic center (Blitz et al. 1993). The bar structure of the bulge is requisite for infalling the gases to the central nuclear cluster containing the central black hole (Regan & Teuben 2004). Though a considerable amount of theoretical and observational works have been made for understanding the central part of the Galaxy, it is still not very clear how the stars revolve around the Galactic center (GC) in the bar-like

potential, and how they play in feedback loops of reincarnation through the star-forming gas clouds to the bar structure.

In theories, stellar orbits in the bar-like bulges are mainly composed of the x_1 and x_2 families, which fabricate the bar with two elongated features along and perpendicular to the bar (Contopoulos, Grosbøl 1989; Sellwood & Wilkinson 1993; Binney, Merrifield 1998). In the past studies, the large-scale bar structure with $\sim 3:1$ elongation, which appears to make an angle of $\sim 30^\circ$ from the Sun-GC direction, revealed in the distribution of infrared sources (Nakada et al. 1991; Blitz, Spergel 1991; Dwek et al. 1995; Nikolaev, Weinberg 1997; Babusiaux,

Gilmore 2005), and other objects (Paczynski et al. 1994). Moreover, the position-velocity diagrams of the CO, ^{13}CO , and HI gas distributions clearly indicate the presence of such inner-bar structure (Binney et al. 1991; Weiner, Sellwood 1999). However, the inner structure corresponding to the x_2 orbits did not clearly reveal in the near-infrared COBE maps (Binney, Gerhard 1996; Launhardt et al. 2002). Recently, Alard (2001) and Nishiyama et al. (2005) analyzed the NIR photometric data of stars toward the inner galactic bulge, finding a presence of the small-scale feature ($|l| < 2^\circ$) which is possibly elongated perpendicularly to the large-scale bar structure.

In order to study kinematics of stars in the Galactic bulge and its relation to the bar dynamics, we performed in this paper a new survey of mass-losing infrared objects in the central part of the Galaxy using SiO maser lines. The SiO maser lines give a precise radial velocity of the central star under mass loss, i.e., the mean velocity of approaching and receding parts of the circumstellar shell (Jewell et al. 1991). Therefore, obtained radial velocities can directly be interpreted as the stellar velocities. Because ages of these AGB stars are $\sim 0.2\text{--}1$ Gyr (Mouhcine, Lançon 2002), they are dynamically relaxed in the bulge (Arad & Johansson 2001), and therefore can be used as good tracers of the velocity field of the bar-like bulge.

A number of studies of stellar maser sources have been made toward the central part of the Galaxy (Lindqvist et al. 1992; Izumiura et al. 1995; Sjouwerman et al. 1998; Deguchi et al. 2000; Deguchi et al. 2004a). This paper particularly focuses on the area of the inner bar region ($|l| < 3.5^\circ$, and $|b| < 1^\circ$). Because the IRAS survey was very incomplete in this region due to source confusion in the high source density area, the previous SiO survey based on the IRAS catalog in this region (Deguchi et al. 2000 ; $|l| < 3^\circ$, and $|b| < 3^\circ$) sampled the objects at more or less higher latitudes ($|b| \gtrsim 1^\circ$). Furthermore, the other unbiased surveys (non-targeted surveys; Shiki et al. 1997; Miyazaki et al. 2001; Deguchi et al. 2002) inevitably focused on the much smaller areas near the galactic center.

This paper presents the result of SiO maser survey of MSX/2MASS objects in the area $|l| < 3.5^\circ$, and $|b| < 1^\circ$. The source sampling was made based on the MSX and 2MASS catalogs: the MSX catalog (Price et al. 2001) provides a large number ($\gg 1000$) of middle-infrared sources in the above area, except very near to the galactic center ($\lesssim 10'$). With 2MASS identifications, the AGB stars under mass loss are easily picked up effectively excluding young stellar objects from the sample. These objects are used as dynamical tracers in the inner bar region of the Galaxy. Because the SiO survey of the very central area ($|l|$ and $|b| \lesssim 15'$; inner ~ 30 pc) have already finished (Imai et al. 2002; Deguchi et al. 2004a), we excluded the central $15'$ area from the present survey.

2. Observations and results

Simultaneous observations in the SiO $J=1-0$, $v=1$ and 2 transitions at 43.122 and 42.821 GHz, respectively, were made with the 45-m radio telescope at Nobeyama during the periods of 2004 February–May, and 2005 February–May. Prior to the main long-term project of 2004–2005, a pilot study of about ten sources for this project was made in May 2003; detections in this pilot study were also involved in this paper. We used a cooled SIS mixer receiver (S40) for the 43 GHz observations and accousto-optical spectrometer arrays, AOS-H and AOS-W, having bandwidths of 40 and 250 MHz with 2048 channels each; the effective velocity resolution of the AOS-H spectrometer was 0.3 km s^{-1} . They covered the velocity range of $\pm 390 \text{ km s}^{-1}$, for both the SiO $J=1-0$ $v=1$ and 2 transitions. The overall system temperature was between 200 and 300 K, depending on the weather condition. The half-power telescope beam width (HPBW) was about $40''$. The antenna temperature given in the present paper is that corrected for the atmospheric and telescope ohmic loss, but not for the beam or aperture efficiency ($\equiv T_a^*$). The conversion factor of the antenna temperature to the flux density is about 2.9 Jy K^{-1} . To save observation time, we employed a position-switching sequence, Off–On1–On2–On3 to observe three objects at once, where the off position was taken $7'$ west of the first-object position (On1) in right ascension; the separation of the off position corresponds to the angle moved by an object in the sky during the typical integration (20 s), additional telescope-slewing, and settling time (10 s), so that the integrations were made nearly at the same elevation angle. With this sequence, we saved about 50% of the total observation time compared with the time of simple On–Off sequences. Further details of SiO maser observations using the NRO 45-m telescope have been described elsewhere (Deguchi et al. 2000), and are not repeated here.

The source selection was made from the MSX and 2MASS catalog, by applying the following criteria:

1. $|l| < 3.5^\circ$ and $|b| < 1^\circ$.
2. MSX objects brighter than $F_C = 1.75 \text{ Jy}$ (with $F_E > 0$) with 2MASS NIR counterparts within $8''$, where F_C and F_E are the flux densities in the MSX C ($12\mu\text{m}$) and E ($21\mu\text{m}$) bands, respectively.
3. $K < 11.5$, $H - K > 1.0$, and $K < 6.0 + 1.6 \times (H - K)$ for the 2MASS counterparts.

The similar criteria except (1) have been used for the previous SiO maser searches in the Galactic disk (Nakashima, Deguchi 2003; Deguchi et al. 2004b) and are approved to be quite effective for picking up the mass-losing AGB stars with SiO masers, though a small number of young stellar objects, which have similar colors, inevitably contaminate the sample. From the sample, we excluded several objects which were already surveyed in the same SiO lines (listed in Table 4). We included these objects for the statistical analysis in section 3 (except J17512667–2825371=IRAS17482–2824, which is apparently a foreground object), but not involved in this sec-

tion.

We also observed a few, additional interesting objects in this area for the sake of completeness; they did not necessarily satisfy the above criteria. These are known OH 1612 MHz sources, bright NIR objects, and bright MSX objects with dubious NIR counterparts.

In total, we observed 291 objects in the area of $7^\circ \times 2^\circ$ of the Galactic center, resulting in 163 detections in the SiO $J = 1-0$ $v = 1$ or 2 transitions. The observational results are summarized in Tables 1 (detections) and 2 (nondetections). Because the positional accuracy of objects in the 2MASS catalog ($\sim 0.1''$) is better than that of MSX sources (a few arc second), we used the 2MASS positions for all of the observed objects except for a few sources (which were observed in the 2003 pilot study). Therefore, we used the 2MASS conventional names for object designation. Table 3 summarizes the infrared properties of the observed sources, listing the 2MASS designation, MSX(6C) designation, separation between 2MASS and MSX objects, 2MASS K magnitude, 2MASS $J - H$, 2MASS $H - K$, MSX flux density in band C ($12 \mu\text{m}$), and MSX color [$= \log(F_E/F_C)$], the radial velocity of SiO, the nearest IRAS source within $60''$, and the separation between the 2MASS and IRAS sources. The details of the spectral features and individual objects are given in Appendix.

The distribution of the sources in the selected area is shown in figure 1. Though the source selection was not biased in the galactic latitude b , the detections (filled circles in figure 1) were found more in the upper half of the l - b plane. This is probably because dense clouds exist more in the $b < 0$ side. The $5^\circ \times 2^\circ$ combined atlas of 2MASS and MSX images¹ gives several silhouettes against background dust emission at the positions coinciding with the source deficient regions in figure 1 around $(l, b) = (-2.3^\circ, -0.7^\circ)$, $(-1.7^\circ, -0.2^\circ)$, $(-0.7^\circ, 0.6^\circ)$, $(0.2^\circ, -0.6^\circ)$, $(0.8^\circ, -0.5^\circ)$, and $(1.7^\circ, -0.3^\circ)$; in these area, source densities in the present sample show an apparent decrease (see figure 1). The clouds seen in silhouettes have been considered to be cold dense clouds without massive star formation (Carey et al. 1998). Though mapping of dense molecular-clouds toward the galactic center, for example, in CS lines does not indicate very large asymmetry with respect to the galactic plane (see figure 2a of Tsuboi et al. 1999), the distribution of cold dense clouds, which was revealed by the MSX survey, seems apparently more abundant in the $b < 0$ side. Furthermore the 2MASS atlas, which was noted above, does not seem to show strong asymmetry in b .² However, this is probably for the background level adjustment in making the atlas.

Figure 2 exhibits the NIR magnitude–color (left) and two-color (right) diagrams of the observed objects. In the two-color diagram, objects falling in the area $(J - H) \lesssim (H - K)$ are normally not O-rich AGB stars. However, because of the blending of stars due to the high star density

toward the Galactic center, 2MASS photometry does not necessarily give accurate magnitudes. Therefore, we did not exclude the objects falling in this "forbidden" area (a lower right part of the right panel of figure 2) from the sample; in fact, we detected many objects in SiO maser lines; this effect was already studied by Deguchi et al. (2004b).

Figure 3 exhibits the MIR flux-density–color (left) and two-color (right) diagrams of the observed sources. Here, the MIR colors are defined as $C_{AC} = \log(F_C/F_A)$ and $C_{CE} = \log(F_E/F_C)$, where F_A , F_C and F_E are MSX flux densities at 8 , 12 and $21 \mu\text{m}$ (bands A, C, and E), respectively. Because the IRAS survey was incomplete in this sky area due to source confusion, and because the MSX survey sensitivities are considerably different in each band (band A is most sensitive), it is interesting to check whether the MIR color–detection rate relations still keep for the present MSX-based sample. The right panel of Figure 3 indicates that the SiO detected sources are peaked around $(C_{CE}, C_{AE}) = (-0.05, 0.14)$, corresponding to the blackbody temperatures of about 360 and 400 K, which seems slightly higher than the temperature obtained from the SiO detection rate of IRAS sources (~ 300 K for $C_{12} \simeq 0$ [$= \log(F_{25}/F_{12})$]; Izumiura et al. 1995). Figure 4 exhibits a histogram of the MIR color, C_{CE} , and a line graph of SiO detection rate. The detection rate seems to be flat (at about 60%) between $-0.4 - 0.2$ in C_{CE} , and drops at both edges, reminding the same tendency of the SiO detection rates which have been found already by observations of IRAS sources (Izumiura et al. 1995; Deguchi et al. 2000). These graphs assure that the sampling for SiO search was made correctly, aiming objects with a maximum SiO detection rate.

The extinction-corrected K magnitude (both for interstellar and circumstellar extinctions) for an individual object can be calculated from the corrected K-band magnitude,

$$K_{H-K} = K - [A_K/E(H-K)][(H-K) - (H-K)_0], \quad (1)$$

where A_K and $E(H-K)$ are the extinction in the K band (both in interstellar and circumstellar) and the difference of extinctions at H and K bands (Whitelock et al. 1991). Nishiyama et al. (2005) gave $A_K/E(H-K) = 1.4$ for NIR objects toward the Galactic Center. Therefore we use this value for the calculation of the corrected K-band magnitude later on. We also assume that $(H-K)_0 = 0.5$, corresponding to the M6III star without interstellar and circumstellar extinction (Zombeck 1990). If the absolute bolometric magnitude is constant for the sampled objects, the corrected K magnitude, K_{H-K} , can be regarded as an indicator of the distance. The histogram of K_{H-K} of the present sample is shown in figure 5 with the SiO detection rate (line graph). The peak of the histogram occurs at $K = 5.5 - 6.0$. Note that the M6III star without extinction should have $K \sim 5.5$ at the distance of 8 kpc. Considering these facts, we believe that a majority of the sampled objects are located at the distances similar to that of the galactic center, i.e., in the Galactic bulge. Of course, a few bright objects with $K_{H-K} < 4$, or $F_C > 12$

¹ available at http://www.ipac.caltech.edu/2mass/gallery/2mass_msx_gcatalog.jpg

² see http://www.ipac.caltech.edu/2mass/gallery/2mass_msx_gc.html

Jy are probably foreground objects: they were excluded from the sample in the analysis of the velocity field in the next section.

We checked the previous OH 1612 MHz or H₂O 22.235 GHz maser objects in the same area. Table 5 summarizes the results: 14 objects (these are mostly detected by the VLA or ATCA observations) are found to lie within a few arc seconds from the sampled objects, except OH357.77–00.15, which was a single-dish detection (Caswell et al. 1981). The radial velocities of the OH 1612 MHz objects coincide well with those of SiO except one case, OH358.720–00.620, which was a single peak detection (Sevenster et al. 1997) of receding side of the expanding shell.

3. Discussion

3.1. Longitude–velocity diagram : overall structure

The radial velocities of the 163 SiO detected objects with additional 5 previous detections in table 4 (except IRAS 17482–2824 for a probable foreground object) are plotted against Galactic longitude in figure 6. The CO $J=1-0$ $l-v$ map (Dame et al. 2001) and the map of the x_1 and x_2 orbits in a bar potential (Bissantz et al. 2003) are overlaid in figures 6a and 6b, respectively. The SiO and CO distributions seem to be moderately correlated: the source-sparse regions (we often called these as "holes" in previous papers; Izumiura et al. 1995) are seen around $(l, V_{\text{lsr}})=(-2.4^\circ, 30 \text{ km s}^{-1})$, and $(-2.2^\circ, -120 \text{ km s}^{-1})$, where the CO map (which indicates gas distribution toward the same direction) also gives a low emission intensity. More SiO sparse regions are seen around $(1.5^\circ, 50 \text{ km s}^{-1})$ and $(-0.5^\circ, 30 \text{ km s}^{-1})$, which coincide with the vacant regions of the x_1 and x_2 trajectories in figure 6b. These features are considered to be observational signatures of bar dynamics (Kuijken, Merrifield 1995). However, a large difference between the SiO and CO distributions is recognized at the extreme high velocity part, i.e., outer envelope of the CO features; SiO objects are seen beyond the upper and lower limits of the radial velocity of the CO gas, which will be discussed in the next section. In addition, no strong feature in the SiO distribution is found for the velocities corresponding the 240 pc molecular ring (cf. Binney et al. 1991; Sawada et al. 2004).

Furthermore, figure 6a indicates that more SiO objects appear at the negative velocity side than at the positive velocity side (113 against 55, respectively). This asymmetry of the source velocity distribution has already been noticed in Izumiura et al. (1995) and Deguchi et al. (2000); this phenomenon has been seen in all of the SiO maser velocity data toward the Galactic bulge. This is attributed to the preferential detection of the bulge foreside objects: the foreside (to the Galactic center) stars tend to have negative radial velocities and backside stars tend to have positive radial velocities due to bulge streaming motion in the x_1 orbits; preferential detections of the foreside sources with the telescope sensitivity reaching to the Galactic center objects make more objects with the negative velocities.

The other notable feature in figure 6 is a rough alignment of the objects along the line $V_{\text{lsr}} \sim 100 \times (l/\text{deg}) \text{ km s}^{-1}$ (which is shown as the red broken line in figure 7b) at the range $|l| < 1.5^\circ$, which roughly coincides with the x_2 orbit trajectories. This feature was not seen in the $l-v$ map of IRAS/SiO objects in $|l| < 3^\circ$ and $|b| < 3^\circ$ (figure 6 of Deguchi et al. 2000), in which the survey based on IRAS catalog was quite incomplete in $|b| < 1^\circ$. Therefore, it is highly likely that these are objects in the x_2 orbits. A full discussion of these objects will be given in Section 3.3.

Figures 7ab illustrate the high-velocity group of stars outside of the x_1 orbits and the low velocity group which presumably belongs to the x_2 orbit family. The boundary was drawn somewhat arbitrarily, though the source distributions and the model orbits were taken into account.

3.2. High-velocity objects in the longitude–velocity diagram

Figure 7a depicts the eccentric-group objects in the $l-v$ diagram. These objects are chosen because of their positions out of x_1 orbit trajectories. They cannot belong to the normal outer x_1 orbits, because the x_1 orbits with larger apocenter distances take smaller $|V_{\text{lsr}}|$ in the $l-v$ diagram, where the trajectories of such orbits are extended to the middle-right to middle-left (with an inclination due to a rotational motion) as shown in figure 6b.

Note that the high-velocity objects were found at very inside ($|l| \sim$ a few arcminutes from the Galactic center; van Langevelde et al. 1992; Deguchi et al. 2004a) to the outside, i.e., $|l| \sim 3^\circ$ out of the molecular ring at $R = \sim 240$ pc. They are presumably in the orbits with peri- and apo-center distances of ~ 0.01 and $\gtrsim 1.5$ kpc, respectively, gaining a large kinetic energy with converting the potential energy. Because a stellar system is collisionless, their orbits can be intersected, even though such orbits are forbidden in the gas dynamics (e.g., Binney et al. 1991); the intersection of orbits causes strong shock in gas dynamics, quickly infalling gases to the inside (Contopoulos et al. 1989).

An inferred trajectory of the eccentric group in the $l-v$ diagram (figure 7a), which is suggested from the SiO observation in the present paper, is shown in thick blue lines. We suggest that these are the objects in highly eccentric orbits along the bar with higher speed than normal x_1 orbit family (as shown in the lower left panel in figure 10). In this model, the orbit is prograde; the object in front of the galactic center should exhibits a large negative radial velocity and the object behind should show a large positive velocity.

In order to check the above hypothesis, we have calculated the average extinction-corrected K magnitude, K_{H-K} , for the eccentric group in present SiO sample. The statistical analyses are summarized in Table 6. We divided the 22 SiO eccentric objects into two groups: one with $V_{\text{lsr}} < 0$ and the other with $V_{\text{lsr}} > 0$ (upper and lower parts in figure 7a). Figure 8 shows a histogram of K_{H-K} for each group. We obtain $[K_{H-K}]_{\text{ave}} = 5.7$ and 6.0 for the $V_{\text{lsr}} < 0$ and > 0 groups, respectively. Therefore, we again

Fig. 1. Source distribution in the galactic coordinates. The filled and unfilled circles indicate the SiO detections and nondetections. The inclined central square indicates the region already surveyed by Deguchi et al. (2004a).

Fig. 2. Near-IR magnitude-color (left panel) and two-color (right panel) diagrams. The filled and unfilled circles indicate the SiO detections and nondetections.

Fig. 3. Middle-IR flux-color (left panel) and two-color (right panel) diagrams. The filled and unfilled circles indicate the SiO detections and nondetections.

Fig. 4. Histogram of the MIR-color, $C_{CE} = \log(F_E/F_C)$. The line graph shows the SiO detection rate (with probable uncertainty). The shaded and unshaded areas indicate the SiO detections and nondetections.

Fig. 5. Histogram of corrected K magnitude, and the SiO detection rate (line graph with uncertainty). The shaded and unshaded areas indicate the SiO detections and nondetections.

confirmed the tendency of the negative-velocity objects having larger brightness, though it is not statistically significant because of the small number; the t-test gives a 43 % probability for the null hypothesis of two sets having the same distribution function; in other words, only with 57 % of the confidence level, we can state that the average K_{H-K} are different between the two sets.

In order to have higher confidence level in statistics, we have added 9 similar high-velocity eccentric objects in $|l| < 3^\circ$ and $|b| < 3^\circ$, which was found in the previous SiO survey (Deguchi et al. 2000). The results are summarized in the middle rows of table 6. With slight increasing numbers of the sets, the statistical confidence level increases up to 66 %. Furthermore, even if we added the other 15 eccentric objects (with 2MASS K -band identification), which were found by OH 1612 MHz survey in the same area (Sevenster et al. 1997), the statistical confidence does not increase significantly. In fact, the addition of OH 1612 MHz causes a significant increase of $[K_{H-K}]_{\text{ave}}$ for both groups, as shown in table 6. Therefore, the NIR property of the OH 1612 MHz objects (detected by Sevenster et al. 1997) is inferred considerably different from the SiO masering objects, probably due to contamination by post-AGB objects (or even by young stellar objects) to the sample. In fact, 2/3 of the sampled OH high-velocity objects are at higher latitudes ($1^\circ < |b| < 3^\circ$), suggesting that high velocity objects appear at considerably higher latitudes in the Galactic bulge (even higher than $|b| > 3^\circ$ as suggested by higher-latitude SiO maser surveys; Izumiura et al. 1995).

Above analyses revealed the tendency of the negative (or positive) high velocity objects being in front of (or behind) the Galactic center, although it is not statistically

very significant. One reason for obtaining this indecisive result seems to stem from the use of 2MASS K magnitudes which were given only in one-time measurements. Because SiO masing objects are mostly large-amplitude variables as miras and semiregulars (for example, see Deguchi et al. 2004a), the average of K_{H-K} in the present sample inevitably involve uncertainty of about 1 magnitude (see Glass et al. 2001). We believe that, if the K magnitude averaged over a light variation period is used, a significant improvement will be obtained in the statistical analysis. The other factor of uncertainty may be involved in the 2MASS photometric measurement due to blending of the star images. However, because of the small number, exclusion of these low-quality objects does not improve the situation in the present data.

The velocity distribution of stars in the bar-like bulge can be interpreted in terms of the periodic orbits which compose the bar potential (Schwarzschild 1979). A number of theoretical studies of the stellar orbits in the barred spiral galaxies revealed that there are stable periodic orbits called as the x_1 and x_2 orbit families (Contopoulos 1988; Athanassoula 1992) with additional higher-order resonance family and the other stationary-orbit family in which a particle moves around the periodic orbits. (Bureau, Athanassoula 1999; Bureau, Athanassoula 2005). Dynamical models for the Galactic bulge have been built with Schwartzschild's galaxy building technique (Zhao 1996; Häfner et al. 2000; Bissantz et al. 2004). However, a rigorous comparison of the model velocity fields or distribution function with observational ones has still been lacked. According to the model created by Zhao (1996), 55% of stars in the bulge belong to the direct regular (mostly x_1) orbits, and the other 45%

Fig. 6. a. SiO longitude-velocity diagram overlaid on the CO $l-v$ map (taken from Dame et al. 2001). Note that SiO represents a stellar motion, while CO represents a gas motion. The large circle indicates a foreground object. The 240 pc molecular gas ring feature is faintly seen in the CO map, tracing a parallelogram through the points, $(2^\circ, 220 \text{ km s}^{-1})$, $(-1^\circ, 100 \text{ km s}^{-1})$, $(-2^\circ, -220 \text{ km s}^{-1})$, and $(1^\circ, -100 \text{ km s}^{-1})$ (cf. figure 6b).

Fig. 6. b. SiO longitude-velocity diagram overlaid on the x_1 and x_2 orbit trajectories [taken from figure 11 of Bissantz et al. (2003)]. The large circle indicates a foreground object. Thin outer curves spreading between $V_{\text{lsr}} = \pm 240 \text{ km s}^{-1}$ are trajectories for the x_1 orbit family, and inner curves concentrating between $V_{\text{lsr}} = \pm 85 \text{ km s}^{-1}$ and between $l = \pm 1.2^\circ$ are those for x_2 orbit family.



Fig. 7. a. longitude–velocity diagram for the eccentric objects (left panel). Filled circle and open square indicate SiO- and OH-detected objects, respectively. The blue segments of lines in the left panel are parts of a trial trajectory deducing the spatial orbits. Two objects (filled circle with open square) are of both SiO and OH detections.

of stars are in composite (irregular and retrograde) orbits. The dynamical model created by Häfner et al. (2000) suggested a slight enhancement of mass distribution of stars at near-zero angular momenta with considerable high energies (figure 12 of Häfner et al. 2000), though exact percentage of these stars and their spatial orbits were not given explicitly. It is desirable to compare the fraction of these low angular-momentum objects in these numerical models with the present result in future. More discussion on this issue is given in Appendix B.

3.3. Inner-bar objects in the longitude–velocity diagram

As described in section 3.1, we find a rough alignment of stars to the straight line (near the x_2 -family orbits ; figure 6b). A similar feature was seen in the l – v diagram of OH 1612 MHz data subset ($|l| < 1^\circ$ and $|b| < 0.5^\circ$; Sevenster et al. 1997), which was shown clearly in figure 8 of Deguchi et al. 2000 in filled symbols. The feature seems to appear less clearly in the lower right quadrant of figure 6b, because the x_1 -family objects are expected to contaminate the sample more in the negative radial velocity than in the positive radial velocity.

We depicted the part of l – v diagram in figure 7b, prescribing the boundaries of the x_2 orbit feature based on

the following considerations. Because of the concentration of 6 objects at the upper area, $0^\circ < l < 1.5^\circ$ and $100 < V_{\text{lsr}} < 150 \text{ km s}^{-1}$, we designated these also in the x_2 family, though the theoretical curves for the x_2 family shown in figure 6b (Bissantz et al. 2003) reach only up to $V_{\text{lsr}} = 80 \text{ km s}^{-1}$. In fact, the x_2 orbits in the models of Englmaier & Gerhard (1999) extend up to ± 120 – 140 km s^{-1} in their figures 13 and 14. The difference from Bissantz et al. (2003) seems to stem from the rapid rise of rotation curve at the inner 300 pc in the Englmaier & Gerhard (1999)'s model. Therefore, a considerable freedom seems to exist in dynamical models for the limiting stellar velocities in x_2 orbits, though some constraints can be obtained from CO gas observations (e.g., Stark et al. 2004). Furthermore, stellar (composite) orbits can possibly be extended beyond the outer boundary of gas x_2 orbits.

Numerical model calculations predicted a very low fraction (less than 1 %) of x_2 orbits stars among the whole bulge stars (Zhao 1996; Häfner et al. 2000). However, the present SiO observation seems to give more than a few percent of stars belong to the x_2 orbit family, though exact evaluation of the fraction is somewhat difficult due to lower survey completeness of SiO maser sources at the

Fig. 7. b. longitude–velocity diagram for the inner-bar objects with SiO masers. Open and filled circles indicate the suggested x_1 and x_2 orbit objects. The red solid lines indicate the boundaries of subsets for the orbital families, and the red broken line indicates a separation for the fore and back sides of the x_2 orbits (see the right panels of figure 10).

Fig. 8. Histogram of K_{H-K} for the eccentric-group objects. The shaded and unshaded areas indicate the $V_{\text{lsr}} > 0$ and $V_{\text{lsr}} < 0$ sets.

outer part of the bulge. Moreover, the boundary drawing in figure 7b is slightly subjective. Therefore, we made a statistical analysis for the designated object sets and checked the validity of grouping in figure 7b.

We performed the following two statistical tests. The first check is the latitude distribution for the two sets: one for the supposed x_2 family set (filled circles in figure 7b), and the other for the supposed x_1 family set (open circles in figure 7b). It is expected that the x_2 family orbits are centrally condensed inside the x_1 orbits. Therefore, the x_2 family objects spread less in Galactic latitude. The first two rows of table 7 summarize the result of statistical analysis: the average of $|b|$ for the supposed x_2 family set is 0.40° ($\pm 0.31^\circ$) while that for the supposed x_1 family set is 0.53° ($\pm 0.27^\circ$). The t-test gives the probability of 0.10 for the null hypothesis of two sets having identical distribution functions. In the other words, we can state with a probability of more than 90% that the selected x_2 family set is more concentrated to the galactic plane than the selected x_1 family set is.

Above analysis indicates that the selection of the x_2 family objects is made roughly correctly, though the x_1 family objects may contaminate the x_2 family set in some degree (the opposite is less likely). Therefore, we investigated further whether or not evidence appears on the depth difference along the line of sight for these objects. We separated the sample into 4 sets: the foreground x_1 -family set, the background x_2 -family set, the foreground x_2 -family set, and the background x_1 -family set (most left, next left, next right, most right in figure 7b [the x_2 -family set deviated into two by the broken line]; see the spatial geometry in the lower right panel of figure 10). The result is shown after the 3rd raw of Table 7. In these sets, set 1 has brightest K_{H-K} , and set 2 has faintest K_{H-K} . The t-test gives that the difference of K_{H-K} between set 1 and set 2 is statistically significant with the 90% significance level, though not for other pairs of the sets.

In this analysis, it is robust that there is a significant difference of about ~ 0.5 mag in mean K_{H-K} mag for the foreside x_1 family objects from others. This value corresponds to the distance ratio of about a factor of 1.25, indicating that the set-1 objects are located at distance of 6.4 kpc from the Sun on the average if we assume the distance of 8 kpc for the other sets (average of sets 2 and 3) of objects. It is not clear why the average K_{H-K} of the set 4 is brighter than the average K_{H-K} of set 2. It may be due to statistical fluctuation by the small number of set 4, or contamination by members in composite-orbit families.

4. Conclusion

We surveyed the MSX/2MASS objects in the sky area of $|l| < 3.5^\circ$ and $|b| < 1^\circ$ in the 43 GHz SiO maser lines and obtained accurate radial velocities of the detected 163 objects. The $l-v$ diagram of this sample clearly revealed the x_2 orbit family feature at the positive velocity side. Furthermore, an eccentric velocity feature, which cannot be attributed to the x_1 orbit family, appears on the same

diagram. The extinction-corrected K magnitude (a distance modulus when subtracted by absolute magnitude), indicates a sequential deposition of these feature sets if we properly assign the fore and back sides of the bulge-bar objects from their radial velocities. Though the statistical tests do not necessarily give significant results except a few cases, the tendency appeared in the distance modulus is consistent with the dynamical model using periodic orbits in the bulge bar. We conclude that the measurements of average K magnitudes over light-variation periods will be useful for further accurate determination of the distance, as well as the presentation of the periodic orbits on the position-velocity diagram will be for comparison with the observations.

The authors thank Dr. T. Omodaka, and his students for the help of observations and encouragements. They also thank Drs. T. Sawada and J. Koda for useful discussions. This research made use of the SIMBAD and VizieR databases operated at CDS, Strasbourg, France, and as well as use of data products from Two Micron All Sky Survey, which is a joint project of the University of Massachusetts and Infrared Processing and Analysis Center/California Institute of Technology, funded by the National Aeronautics and Space Administration and National Science foundation, and from the Midcourse Space Experiment at NASA/IPAC Infrared Science Archive, which is operated by the Jet Propulsion Laboratory, California Institute of Technology, under contract with the National Aeronautics and Space Administration.

Appendix. A. Individual objects

We presented all of the spectra of the SiO $J = 1-0$ $v = 1$ and 2 transitions for the detected objects in figure 9a–j. Here we discuss the individually interesting objects.

- J17404953–3055183 (~OH 357.77–00.15 =IRAS 17375–3053): Doubly peaked OH 1612 MHz object was detected by Parkes 64m telescope ($HPBW \sim 12.5'$ beam) about $37''$ North-East of this object (Caswell et al. 1981), and the position is close to the faint MSX object, G357.7672–00.1451 ($F_C = 0.8$ Jy), and IRAS 17375–3053. However, slightly brighter MSX object with $F_C = 2.4$ Jy, G357.7643–00.1591, is the object that we observed in the present paper. Because Sevenster et al. (1997) did not detect this object with VLA, we do not have accurate positions of this OH source. Because the radial velocity of SiO source differs only by 5.8 km s^{-1} to the center velocity of OH double peaks, we tentatively assigned this object to OH 357.77–00.15 in table 5.
- J17425115–2951513 (=G358.8932+00.0277): This is a bright infrared object with $F_C = 27.2$ Jy with no IRAS counterpart within $1'$. The SiO $J = 1-0$ $v = 1$ spectrum exhibits interesting triple peaks spreading in the velocity span of about 20 km s^{-1} , which may

be an indication of a supergiant with heavy mass loss. No previous OH maser observation was reported for this source.

- J17465905–2817037? (=ISOGAL–P J174659.1–281658=OH .713 +.084): This is a faint OH/IR object which occupies a unique position in the left panel of figure 3 ($K = 11.193$ and $H - K = 1.715$), where it is out of the area aimed in the present SiO survey. This object was observed because of the previous OH detection (Lindqvist et al. 1992) and its peculiar characteristic in the $K - H - K$ diagram. The SiO radial velocity, 98.4 km s^{-1} , agrees well with the center velocity of OH double-peaks, 96.8 km s^{-1} .
- J17481382–2725523 (=G001.5844+00.2889 =IRAS 17450–2724): This is a bright IR source with $F_C = 44.8 \text{ Jy}$ and IRAS LRS class of 13 (no clear spectral feature). This object was observed for the sake of completeness in this SiO survey. SiO maser emission was detected first time in this survey at $V_{lsr} = -29.5 \text{ km s}^{-1}$, identifying this object as an O-rich evolved star. No OH 1612 MHz line has ever been detected.
- J17520868–2711412 (=G002.2335–00.3360 =IRAS 17490–2711): This is a bright IR source with $F_C = 15.7 \text{ Jy}$. SiO maser emission was detected first time in this survey at $V_{lsr} = -81.5 \text{ km s}^{-1}$, identifying this object as an O-rich evolved star.

Appendix. B. Approximate Orbits

From the deduced trajectory in the $l-v$ diagram (figures 7ab), we can draw an approximate orbital curve on the 2D coordinate system corotating with a bar. Here we assume that a pattern velocity of the bar, $\Omega_p = 60 \text{ km s}^{-1}$ (Bissantz et al. 2003). The particle position on the line of sight can be written as

$$Y = Y_0 + \int V_Y dt = Y_0 + \int V_Y / V_X dX. \quad (2)$$

Here the Y axis is taken along the line of sight toward the galactic center and the X axis is taken to be perpendicular to the Y axis on the galactic plane, and V_X , and V_y are the velocity components on the X and Y directions on the co-rotating system, respectively, and Y_0 is the integration constant. The velocity, V_Y , is given from the assumed trajectory (V_r) as a function of the coordinate X in the corotating system as

$$V_Y \sim V_r - X \Omega_p. \quad (3)$$

Here, V_r is the radial velocity of a star in the rest frame ($\equiv V_{lsr} + V_0 \sin l$, where V_0 and l are the rotational velocity of the Local Standard of Rest and the Galactic longitude, respectively). Because the velocity perpendicular to the line of sight, V_X , is unknown, we assume for simplicity that V_X is constant on each segment of the trajectory. Then, equation (2) indicates that the linear segment of the trajectory in the $l-v$ diagram is expressed by a part of parabola in the $X-Y$ coordinates. The four linear segments of the trajectory (upper panel of fig 10) can

be drawn as a closed loop of four segments of parabola as shown in the lower panel of figure 10. (Because the straight dotted lines connecting the upper and lower edges in the upper-left panel are just a first guess, they are not verified except for the case of the 2:1 resonance. For the case of 4:1 resonance, these parts are inferred to be complex crossed curves.)

Because the assumption of constant V_X is not exactly hold for the realistic cases, an orbit obtained with this method is quite approximate. However, the obtained looped orbit correctly shows an elongation along the large scale bar major axis, and four corners of the orbit suggesting correctly the self-crossing looped orbit, even though the width of the loop can vary with arbitrary choice of constant value of V_X . The obtained loop orbit is similar to the x_1 family orbits shown in figure 6 of Skokos et al. (2002), or self-crossing orbits in the figure 13 of Regan & Teuben (2004). However, because the orbits, which are inferred from the observation, do not satisfy any dynamical requirements, the stars on these orbits may not necessarily rotate at the bar pattern speed in a longer time scale. The difference of the pattern speed makes the pericenter precession, and a real orbit is likely to be a non-closing loop. Such a precessing orbital motion makes the limiting radial velocities smaller (with making large angles to the line of sight from the Sun), as illustrated by the broken lines in the upper-left panel in figure 10 (for example of a dynamical model, see figures 4–6 of Pichardo et al. 2004). In the case when the precessing motion is rapid (higher-order resonance or composite orbits), the particle density in the $l-v$ diagram tends to be homogeneous in the broken square in the upper-left panel in figure 10. With such highly irregular or composite orbits, it may be hard to explain the presence of "holes" in the $l-v$ diagram as shown in figure 6. Therefore, the slow-precession, as for the 4:1 resonance family orbits (as illustrated by Contopoulos 1988; Kaufmann & Patsis 2005), would be preferable as an explanation of the eccentric group of stars.

References

- Alard, C. 2001, A&A, 379, L44
 Arad, I., & Johansson, P. H. 2005, MNRAS, 362, 252
 Athanassoula, E., 1992, MNRAS, 259, 328
 Babusiaux, C. & Gilmore, G., 2005, MNRAS, 358, 1309
 Binney, J., Gerhard, O. E., Stark, A. A., Bally, J., & Uchida, K. I. 1991, MNRAS, 252, 210
 Binney, J., & Gerhard, O. E. 1996, MNRAS, 279, 1005
 Binney, J., & Merrifield, M. 1998, Galactic Astronomy (Princeton Univ. Press, Princeton), 588
 Bissantz, N., Englmaier, P. & Gerhard, O. 2003, MNRAS, 340, 949
 Bissantz, N., Debattista, V. P., & Gerhard, O. 2004, ApJ, 601, L155
 Bureau, M. & Athanassoula, E. 1999, ApJ, 522, 686B
 Blitz, L., & Spergel, D. N. 1991, ApJ, 379, 631
 Blitz, L., Binney, J., Lo, K. Y., Bally, J., & Ho, P. T. P. 1993, Nature 361, 417
 Bureau, M., & Athanassoula, E. 2005, ApJ, 626, 159B

Fig. 10. Schematic trajectory in the position-velocity diagram (upper panels) and the corresponding spatial orbit in the corotating system (lower panels). The left panels illustrate the case of eccentric-velocity group and the right panels the case of the x_2 orbits. They are assumed to be expressed by the segments of linear trajectory in position-velocity diagram, but in fact, they must be more smoothed curves. The open and filled arrows show the directions of motion. The position-velocity diagram ($X-V_Y$) can be converted to the $l-V_r$ diagram by adding the rotation of the coordinate, $X \Omega_P$. Dotted lines in the left panels are just guesses connecting the upper and lower segments, which may be more complex curves for 4:1 or higher-order resonance orbits. Broken lines in the top left panel indicate the upper and lower limits for the orbits precessing relatively to the bar pattern, which is indicated by broken arrows in the lower-left panel. The Sun is supposed to be located at $(0, -8)$ in the lower panels.

- Caswell, J. L., Haynes, R. F., Goss, W. M., & Mebold, U. 1981, *Aust. J. Phys.*, 34, 333
- Carey, S. J., Clark, F. O., Egan, M. P., Price, S. D., Shipman, R. F., & Kuchar, T. A. 1998, *ApJ*, 508, 721
- Contopoulos, G. 1988, *A&A*, 201, 44
- Contopoulos, G., & Grosbøl, P. 1989, *A&AR*, 1, 261
- Contopoulos, G., Gottesman, S. T., Hunter, J. H., Jr., & England, M. N. 1989, *ApJ*, 343, 608
- Dame, T. M., Hartmann, D., & Thaddeus, P. 2001, *ApJ*, 547, 792
- Deguchi, S., Fujii, T., Izumiura, H., Kameya, O., Nakada, Y., Nakashima, J., Otsubo, T., & Ukita, N. 2000, *ApJS*, 128, 571
- Deguchi, S., Fujii, T., Miyoshi, M., & Nakashima, J. 2002, *PASJ*, 54, 61
- Deguchi, S., Imai, H., Fujii, T., Glass, I., Ita, Y., Izumiura, H., Kameya, O., Miyazaki, A., Nakada, Y., & Nakashima, J. 2004, *PASJ*, 56, 261
- Deguchi, S., Fujii, T., Glass, I., Imai, H., Ita, Y., Izumiura, H., Kameya, O., Miyazaki, A., Nakada, Y., & Nakashima, J. 2004, *PASJ*, 56, 765
- Dwek, E., et al. 1995, *ApJ*, 445, 716
- Englmaier, P. & Gerhard, O. 1999, *MNRAS*, 304, 512
- Glass, I. S., Matsumoto, S., Carter, B. S., & Sekiguchi, K. 2001, *MNRAS* 321, 77
- Habing 1987, in the Galaxy, ed. G. Gilmore & P. Carswell (Dordrecht: Reidel), p173
- Häfner, R., Evans, N. W., Dehnen, W., & Binney, J. 2000, *MNRAS*, 314, 433
- Imai, H., et al. 2002, *PASJ*, 54, L19
- Izumiura, H., Deguchi, S., Hashimoto, O., Nakada, Y., Onaka, T., Ono, T., Ukita, N., & Yamamura, I. 1995, *ApJ*, 453, 837
- Jewell, P. R., Snyder, L. E., Walmsley, C. M., Wilson, T. L., & Gensheimer, P. D. 1991, *A&A* 242, 211
- Kaufmann, D. E., & Patsis, P. A. 2005, *ApJ*, 624, 693
- Kuijken, K. & Merrifield, M.R. 1995, *ApJ*, 443, L13
- Launhardt, R., Zylka, R., & Mezger, P. G. 2002, *A&A*, 384, 112
- Lindqvist, M., Habing, H. J., & Winnberg, A. 1992, *A&A*, 259, 118
- Messineo, M., Habing, H. J., Sjouwerman, L. O., Omont, A., & Menten, K. M. 2002, *A&A*, 393, 115
- Miyazaki, A., Deguchi, S., Tsuboi, M., Kasuga, T., & Takano, S., 2001, *PASJ*, 53, 501
- Mouhcine, M., & Lançon, A. 2002, *A&A*, 393, 149
- Nakada, Y., Deguchi, S., Hashimoto, O., Izumiura, H., Onaka, T., Sekiguchi, K., & Yamamura, I. 1991, *Nature*, 353, 140
- Nakashima, J., & Deguchi, S. 2003, *PASJ*, 55, 203
- Nikolaev, S., & Weinberg, M. D. 1997, *ApJ*, 487, 885
- Nishiyama, S., Nagata, T., Baba, D., Haba, Y., Kadokawa, R., et al. 2005, *ApJ*, 621, L105
- Oka, T., Hasegawa, T., Sato, F., Tsuboi, M., & Miyazaki, A. 1998, *ApJS*, 118, 455
- Paczynski, B., Stanek, K. Z., Udalski, A., Szymanski, M., Kaluzny, J., Kubiak, M., Mateo, M., & Krzeminski, W. 1994, *ApJ*, 435, L113
- Pichardo, B., Martos, M., & Moreno, E. 2004, *ApJ*, 609, 144
- Price, S. D., Egan, M. P., Carey, S. J., Mizuno, D. R., & Kuchar, T. A. 2001, *AJ*, 121, 2819
- Regan, M. W., & Teuben, P. J. 2004, *ApJ*, 600, 595
- Sawada, T., Hasegawa, T., Handa, T., & Cohen, R. J. 2004, *MNRAS*, 349, 1167
- Schwarzschild, M. 1979, *ApJ*, 232, 236
- Sevenster, M. N., Chapman, J. M., Habing, H., Killeen, N. E. B., & Lindqvist, M. 1997, *A&AS*, 122, 79
- Sellwood, J. A. & Wilkinson, A. 1993, *Rep. Prog. Phys.* 56, 173
- Shiki, S., Ohishi, M., & Deguchi, S. 1997, *ApJ*, 478, 206
- Sjouwerman, L. O., van Langevelde, H. J., Winnberg, A., & Habing, H. J. 1998, *A&AS*, 128, 35
- Sjouwerman, L. O., Lindqvist, M., van Langevelde, H. J., & Diamond, P. J. 2002, *A&A*, 391, 967
- Skokos, Ch., Patsis, P. A., & Athanassoula, E. 2002, *MNRAS*, 333, 861
- Stark, A. A., Martin, C. L., Walsh, W. M., Xiao, K., Lane, A. P., & Walker, C. K. 2004, *ApJ*, 614, L41
- Taylor, G. B., Morris, M., & Schulman, E. 1993, *AJ*, 106, 1978
- Tsuboi, M., Handa, T., & Ukita, N. 1999, *ApJS*, 120, 1
- van Langevelde, H. J., Brown, A. G. A., Lindqvist, M., Habing, H. J., & de Zeeuw, P. T. 1992, *A&A*, 261, L17
- Weiner, B. J., & Sellwood, J. A. 1999, *ApJ*, 524, 112
- Whitelock, P., Feast, M., & Catchpole, R. 1991, *MNRAS* 248, 276
- Zhao, H. S. 1996, *MNRAS*, 283, 149
- Zombeck, M. V. 1990, *Handbook of Space Astronomy and Astrophysics* (Cambridge University Press, New York) p70

Table 1. SiO detections.

Name	SiO $J = 1-0$ $v = 1$				SiO $J = 1-0$ $v = 2$				Obs. date (yyymmdd.d)	V_{ave} (km s $^{-1}$)
	V_{peak} (km s $^{-1}$)	T_{peak} (K)	Flux (K km s $^{-1}$)	RMS (K)	V_{peak} (km s $^{-1}$)	T_{peak} (K)	Flux (K km s $^{-1}$)	RMS (K)		
J17352480–3058174	−121.2	0.348	1.034	0.045	−121.8	0.346	0.634	0.048	040225.3	−121.5
J17354457–3134332	59.8	0.461	0.832	0.047	59.8	0.392	0.862	0.061	040422.1	59.8
J17355075–3057569	−270.1	0.306	0.658	0.047	—	—	—	0.048	040225.3	−270.1
J17355648–3140399	−170.0	0.789	3.326	0.047	−168.3	0.714	2.925	0.054	040422.1	−169.1
J17355814–3101029	−67.6	0.178	0.598	0.041	−63.2	0.227	0.500	0.054	040225.3	−65.4
J17355954–3136317	−334.2	0.314	0.436	0.045	−334.5	0.271	0.748	0.057	040422.1	−334.3
J17361848–3038053	−99.3	0.492	2.130	0.045	−98.2	0.451	1.906	0.059	040422.1	−98.7
J17364217–3059117	−145.8	0.296	0.644	0.046	−146.0	0.318	0.935	0.054	040511.0	−145.9
J17371969–3004585	218.8	0.221	0.486	0.051	219.8	0.208	0.801	0.056	050530.0	219.3
J17373917–2959315	−149.5	0.347	0.825	0.049	−149.5	0.385	0.770	0.057	040515.0	−149.5
J17374522–3035313	−144.8	0.232	0.757	0.046	−144.3	0.299	0.930	0.051	040422.1	−144.5
J17374537–3033461	−50.1	0.139	0.467	0.047	−48.1	0.213	0.525	0.061	040422.1	−49.1
J17380035–2955522	32.0	0.300	0.730	0.048	31.1	0.173	0.367	0.066	040515.0	31.6
J17380329–3116094	−308.3	0.230	0.597	0.042	−308.3	0.258	0.746	0.050	040515.1	−308.3
J17380426–3143191	−56.8	0.570	2.719	0.052	−58.6	0.604	2.819	0.069	040515.1	−57.7
J17381197–3046271	−63.1	0.235	0.521	0.048	−63.5	0.198	0.512	0.055	040512.1	−63.3
J17381968–3106094	−71.2	0.124	0.410	0.039	—	—	—	0.051	040421.1	−71.2
J17382060–3056128	−67.6	0.469	1.731	0.072	−68.0	0.639	2.185	0.090	040421.2	−67.8
J17383569–2936372	0.5	0.180	0.789	0.052	4.2	0.291	1.438	0.065	040422.2	2.3
J17384240–3153322	−191.5	0.388	1.161	0.055	−192.6	0.356	0.594	0.063	040515.1	−192.1
J17384424–2926077	96.7	0.210	0.399	0.047	96.0	0.181	0.394	0.056	040421.2	96.3
J17384471–3027057	41.8	0.214	0.429	0.046	40.7	0.262	0.871	0.066	050530.0	41.3
J17385285–3058250	−29.8	0.250	0.610	0.050	−30.1	0.188	0.342	0.059	040519.1	−30.0
J17385873–3023559	−240.4	0.434	1.235	0.052	−239.9	0.176	0.783	0.057	040419.1	−240.2
J17390867–3017183	5.8	0.123	0.110	0.043	1.7	0.206	0.497	0.058	040512.1	3.7
J17391209–2923518	−126.1	0.200	1.004	0.044	−121.7	0.264	0.575	0.054	040421.2	−123.9
J17391903–3011097	−145.2	0.297	0.464	0.044	−148.7	0.176	0.426	0.053	040512.1	−147.0
J17392257–3104456	−193.9	0.255	0.873	0.042	−194.4	0.372	1.110	0.045	040421.1	−194.2
J17394321–2951276	−205.0	0.205	0.510	0.054	−203.9	0.166	0.223	0.063	050527.0	−204.4
J17394506–3055582	50.1	0.309	0.974	0.072	49.9	0.533	0.510	0.092	040421.2	50.0
J17394697–3024485	−190.5	0.392	0.798	0.052	−190.9	0.285	0.538	0.056	040419.1	−190.7
J17395669–2920481	—	—	—	0.046	82.5	0.271	0.743	0.060	040421.2	82.5
J17400034–3114314	75.9	0.229	0.957	0.042	78.7	0.214	0.541	0.060	040515.1	77.3
J17400912–2959191	114.4	0.494	0.806	0.061	114.0	0.409	0.747	0.058	050215.3	114.2
J17401355–2956426	−158.7	0.260	1.764	0.052	−160.6	0.329	1.653	0.062	050527.0	−159.6
J17401688–3032596	−218.9	0.162	0.205	0.043	−221.0	0.262	0.382	0.049	050213.3	−219.9
J17402241–3027273	−318.5	0.291	0.972	0.041	−318.8	0.423	1.180	0.049	050213.3	−318.7
J17403247–2846360	−87.8	0.669	1.974	0.086	−88.2	0.497	1.260	0.114	050530.1	−88.0
J17403670–2933111	−186.1	0.610	1.763	0.056	−186.5	0.496	1.472	0.061	040422.2	−186.3
J17403750–2904098	78.7	0.387	1.077	0.074	79.6	0.366	1.149	0.098	050530.1	79.2
J17404146–3132304	−166.5	0.181	0.950	0.044	−166.6	0.239	0.331	0.049	050212.3	−166.5
J17404825–3050360	−84.8	0.356	1.245	0.051	−84.2	0.346	1.098	0.063	040519.1	−84.5
J17404953–3055183	−87.5	0.344	0.966	0.065	−84.0	0.296	0.707	0.086	050530.1	−85.8
J17405431–3144125	−43.4	0.660	1.888	0.050	−41.0	0.457	1.693	0.061	050524.1	−42.2
J17410791–3159544	174.8	0.410	1.137	0.051	174.2	0.403	1.192	0.048	050212.3	174.5
J17411056–3008096	−128.1	0.571	2.567	0.050	−126.1	0.551	2.682	0.056	040419.2	−127.1
J17411421–2851112	−5.5	0.202	0.699	0.037	−5.3	0.249	0.522	0.046	040418.1	−5.4
J17411489–3000159	68.4	0.344	0.613	0.054	68.0	0.309	1.181	0.067	050215.3	68.2
J17411834–3002290	16.0	0.273	0.642	0.055	15.5	0.242	0.466	0.068	050215.3	15.8
J17413541–2854274	126.0	0.140	0.266	0.041	130.9	0.195	0.187	0.042	040418.1	128.4
J17413828–3145337	22.0	0.326	1.795	0.041	20.1	0.300	1.030	0.058	050212.3	21.1
J17414205–3132063	59.8	0.200	0.719	0.043	58.6	0.273	0.797	0.050	050212.3	59.2
J17414293–3158231	−144.6	0.288	0.892	0.047	−146.3	0.321	0.337	0.054	040511.1	−145.4
J17420881–2955044	−97.2	0.251	1.169	0.055	−92.9	0.303	1.487	0.075	050530.0	−95.0

Table 1. (Continued)

Name	SiO $J = 1-0$ $v = 1$				SiO $J = 1-0$ $v = 2$				Obs. date	V_{ave} (km s $^{-1}$)
	V_{peak} (km s $^{-1}$)	T_{peak} (K)	Flux (K km s $^{-1}$)	RMS (K)	V_{peak} (km s $^{-1}$)	T_{peak} (K)	Flux (K km s $^{-1}$)	RMS (K)		
J17421172-3057189	-6.4	0.163	0.965	0.044	-7.3	0.248	1.219	0.057	050310.3	-6.9
J17421783-2936334	-159.5	0.925	1.953	0.053	-159.7	0.684	1.819	0.064	050213.3	-159.6
J17421887-3015288	-22.9	0.451	2.120	0.055	-25.6	0.458	0.864	0.068	040226.3	-24.2
J17422438-3135073	-107.3	0.279	0.681	0.053	-106.9	0.316	1.233	0.064	050524.1	-107.1
J17424091-3015134	-82.4	0.232	0.528	0.055	-83.0	0.229	0.697	0.068	040226.3	-82.7
J17424480-2932464	—	—	—	0.042	-35.3	0.202	0.363	0.049	050215.3	-35.3
J17425115-2951513†	1.3	2.380	10.032	0.071	-14.6	0.420	0.894	0.095	030513.0	-13.3
J17425616-2931498	-135.6	0.316	2.000	0.045	-140.9	0.218	0.920	0.048	050215.3	-138.3
J17425698-2910005	-20.2	0.204	0.502	0.046	—	—	—	0.058	040519.1	-20.2
J17425995-2957026	-115.8	0.321	0.659	0.052	-116.1	0.566	1.079	0.058	050528.1	-115.9
J17430330-2938016	-52.0	0.312	0.881	0.052	-52.3	0.514	1.335	0.067	050213.3	-52.1
J17430552-3018014	-16.3	0.222	0.805	0.055	-18.6	0.463	2.267	0.070	040226.3	-17.4
J17430981-2924033	-56.7	0.351	1.497	0.059	-53.7	0.345	0.755	0.074	040418.1	-55.2
J17431231-2928496	77.7	0.342	1.055	0.059	73.3	0.351	1.445	0.073	040418.1	75.5
J17432963-2804137	303.7	0.326	0.818	0.056	303.3	0.220	0.870	0.059	050212.4	303.5
J17433271-2915393	-94.3	0.256	0.979	0.049	-94.2	0.488	1.324	0.060	040519.1	-94.2
J17433894-2814165	121.7	0.405	0.621	0.078	118.4	0.481	1.313	0.078	040421.1	120.1
J17435079-2845203	-146.9	0.520	1.510	0.049	-146.8	0.552	1.407	0.055	050215.4	-146.8
J17435211-3057289	-38.6	0.272	0.901	0.044	-38.4	0.290	1.028	0.057	050310.3	-38.5
J17435366-2755443	-142.1	0.174	0.425	0.046	-142.9	0.209	0.689	0.053	050215.2	-142.5
J17435898-2743109	-41.5	0.205	1.231	0.044	-38.7	0.159	0.299	0.055	050214.3	-40.1
J17440282-2740425	125.9	0.303	1.153	0.050	126.4	0.259	0.386	0.050	050214.3	126.1
J17440469-2919538	-48.5	0.471	1.422	0.058	-48.4	0.527	1.339	0.075	040418.1	-48.4
J17440744-2927376†	-200.0	0.169	1.429	0.045	-208.8	0.152	0.408	0.053	030519.1	-204.4
J17441431-2821234	-181.2	0.267	1.281	0.056	-181.6	0.365	0.799	0.069	050212.4	-181.4
J17441640-3039103	-172.8	0.215	0.580	0.045	-172.9	0.213	0.317	0.058	050310.2	-172.8
J17441922-2844217	16.1	0.933	2.607	0.052	16.3	0.779	2.217	0.070	040422.1	16.2
J17443085-2950132	-123.1	0.247	0.486	0.064	—	—	—	0.085	050527.0	-123.1
J17443262-2856120	-65.9	0.327	2.483	0.039	-71.4	0.326	2.786	0.050	050211.3	-68.7
J17443496-2904356†	-5.3	0.623	0.962	0.080	-5.7	0.880	2.454	0.116	030513.1	-5.5
J17443502-3034437	-96.2	0.389	1.981	0.042	-96.3	0.334	1.363	0.059	050310.2	-96.3
J17444943-2757017	-148.8	0.285	0.499	0.045	-149.2	0.344	0.741	0.052	050215.2	-149.0
J17445129-2924548†	-60.0	1.033	8.392	0.122	-61.4	0.835	2.300	0.153	030519.0	-60.7
J17445365-2812464	-79.2	1.611	3.636	0.069	-79.1	1.288	2.806	0.089	040421.1	-79.2
J17445521-2819209	-138.3	0.247	0.512	0.060	-139.9	0.432	1.169	0.071	040511.0	-139.1
J17445788-2957209	-198.3	0.445	2.297	0.057	-197.8	0.594	2.817	0.062	050213.3	-198.0
J17445891-3021064	-38.8	0.218	0.868	0.042	-41.2	0.282	1.437	0.052	040423.1	-40.0
J17451393-2915279	-102.3	0.125	0.405	0.031	-101.1	0.200	0.811	0.038	050211.3	-101.7
J17453430-2747330	-49.6	0.361	1.345	0.045	-50.8	0.533	1.878	0.055	050215.2	-50.2
J17453506-2822467	-54.3	0.751	3.181	0.063	-54.2	0.661	2.542	0.082	040511.0	-54.2
J17454037-2801085	-128.5	0.291	0.456	0.057	-135.8	0.161	0.397	0.062	050525.1	-132.1
J17454130-2746484	-24.4	0.202	0.911	0.046	—	—	—	0.060	040512.0	-24.4
J17454184-2657317	-3.3	0.157	-0.036	0.041	-4.1	0.235	0.636	0.050	040518.0	-3.7
J17454390-2825200	83.0	0.326	0.980	0.065	84.1	0.343	0.857	0.083	050526.1	83.6
J17454949-2933293	57.5	0.152	0.431	0.031	55.6	0.179	0.384	0.045	050211.3	56.6
J17455608-2839274	105.5	0.162	0.582	0.057	105.3	0.544	1.583	0.070	040422.1	105.4
J17455842-2925319	-101.6	0.697	3.712	0.046	-101.7	0.506	3.222	0.060	040518.1	-101.7
J17460233-2803339	-5.0	0.513	2.878	0.059	-0.5	0.706	3.154	0.078	050525.1	-2.8
J17462676-2800037	31.0	0.234	0.980	0.051	35.1	0.309	1.222	0.063	050525.1	33.1
J17465135-2917251	-55.6	0.361	0.979	0.051	-56.4	0.343	0.806	0.063	050528.0	-56.0
J17465644-2726132	-67.7	0.173	0.374	0.038	-67.3	0.177	0.332	0.051	050213.4	-67.5
J17465905-2817037	98.4	0.257	0.916	0.061	98.4	0.388	1.275	0.077	050525.1	98.4
J17465960-2706131	-122.7	0.719	1.503	0.041	-122.4	0.460	0.773	0.057	040423.1	-122.5
J17470149-2755168	141.3	0.193	0.610	0.050	141.5	0.255	0.753	0.049	050524.0	141.4

Table 1. (Continued)

Name	SiO $J = 1-0$ $v = 1$				SiO $J = 1-0$ $v = 2$				Obs. date	V_{ave} (km s $^{-1}$)
	V_{peak} (km s $^{-1}$)	T_{peak} (K)	Flux (K km s $^{-1}$)	RMS (K)	V_{peak} (km s $^{-1}$)	T_{peak} (K)	Flux (K km s $^{-1}$)	RMS (K)		
J17471226–2652362	23.4	0.114	0.416	0.040	21.4	0.152	0.105	0.051	040518.0	22.4
J17471986–2837345	-177.6	0.121	0.381	0.036	-167.9	0.155	0.475	0.041	040418.2	-172.7
J17473221–2807030	-214.6	0.335	0.812	0.065	-214.7	0.321	1.039	0.077	050527.1	-214.7
J17473739–2743116	-37.1	0.237	0.754	0.038	-36.2	0.646	1.728	0.051	050213.4	-36.7
J17473906–2818282	-276.3	0.347	0.456	0.068	-276.8	0.285	0.835	0.082	050527.1	-276.5
J17481087–2920527	9.4	0.255	0.839	0.047	7.8	0.274	1.010	0.064	050528.0	8.6
J17481382–2725523	-29.6	0.152	0.406	0.050	-29.4	0.558	1.335	0.068	050310.3	-29.5
J17481674–2836124	-31.1	0.116	0.285	0.036	-30.4	0.172	0.172	0.046	040418.2	-30.8
J17482755–2829176	-145.2	0.238	0.918	0.055	-145.0	0.383	1.117	0.059	040511.1	-145.1
J17482827–2810434	-186.5	0.309	1.058	0.051	-185.8	0.192	0.796	0.054	050524.0	-186.1
J17483260–2630193	—	—	—	0.049	-173.7	0.277	0.291	0.063	050310.2	-173.7
J17483491–2705072	-214.4	0.128	0.426	0.042	-213.3	0.194	0.569	0.051	040423.1	-213.8
J17483707–2622249	-108.7	0.187	0.618	0.048	-108.3	0.208	0.429	0.062	050310.2	-108.5
J17484102–2749458	-136.6	0.255	0.979	0.052	-141.5	0.508	1.823	0.053	050524.0	-139.0
J17484246–2737518	135.8	0.304	0.408	0.062	135.1	0.189	0.830	0.059	050310.3	135.4
J17484466–2714523	-125.7	0.306	0.934	0.056	—	—	—	0.067	050311.3	-125.7
J17484743–2629591	39.9	0.200	0.813	0.045	40.9	0.191	0.577	0.061	050310.2	40.4
J17485495–2635343	95.8	0.263	0.498	0.039	95.5	0.324	0.847	0.051	040225.2	95.7
J17485855–2858392	72.4	0.236	0.764	0.045	72.0	0.261	0.729	0.054	040423.2	72.2
J17490836–2733293	-114.5	0.198	0.522	0.057	-115.0	0.288	0.282	0.070	050310.3	-114.8
J17493449–2633320	-46.3	0.130	0.214	0.037	-45.2	0.202	0.251	0.050	040225.2	-45.8
J17494622–2857454	187.5	0.231	0.665	0.047	188.5	0.176	0.928	0.044	040423.2	188.0
J17494935–2906177	57.1	0.131	0.374	0.045	57.4	0.194	0.454	0.055	040423.2	57.2
J17495130–2700444	-163.5	0.204	0.459	0.057	-163.9	0.200	0.709	0.066	050528.1	-163.7
J17501702–2845426	25.6	0.890	2.902	0.055	25.7	0.879	2.819	0.072	040511.1	25.7
J17502615–2647048	-92.3	0.467	2.503	0.061	-92.3	0.449	2.035	0.081	040515.0	-92.3
J17502764–2818388	-108.9	0.386	1.155	0.061	—	—	—	0.048	040226.3	-108.9
J17502871–2843472	277.0	0.244	0.733	0.048	275.7	0.220	0.574	0.048	040419.1	276.3
J17502910–2550299	-60.6	0.378	1.535	0.040	-60.2	0.538	1.770	0.050	050212.3	-60.4
J17503133–2803362	129.9	0.446	1.117	0.086	129.3	0.390	0.922	0.089	040515.1	129.6
J17503382–2622283	-52.0	0.282	0.907	0.051	—	—	—	0.069	050310.3	-52.0
J17504394–2840427	96.5	0.294	1.044	0.045	95.6	0.191	0.573	0.055	040419.1	96.1
J17505365–2556283	-36.2	0.184	0.681	0.040	—	—	—	0.057	050212.3	-36.2
J17505401–2709177	8.0	0.557	1.985	0.052	7.7	0.608	2.229	0.067	050213.2	7.9
J17505784–2625025	-105.6	0.228	0.810	0.053	-107.3	0.326	1.347	0.069	050310.3	-106.4
J17510037–2640020	-58.1	0.269	0.683	0.060	-57.6	0.528	1.364	0.079	040515.0	-57.8
J17510408–2718506	21.6	0.169	0.973	0.051	—	—	—	0.067	040226.4	21.6
J17514250–2709204	48.0	0.435	1.291	0.053	47.3	0.475	1.617	0.068	050213.2	47.6
J17514587–2635481	-56.3	0.585	2.137	0.104	-56.2	0.834	2.459	0.138	050526.0	-56.3
J17520753–2628180	15.9	0.453	2.396	0.109	16.1	0.525	0.957	0.137	050526.0	16.0
J17520868–2711412	—	—	—	0.053	-81.5	0.375	0.850	0.070	050213.2	-81.5
J17522130–2720043	273.2	0.361	0.832	0.059	273.9	0.258	0.617	0.056	040226.4	273.6
J17524903–2607386	-164.4	0.616	1.763	0.075	-164.4	0.370	1.579	0.082	050529.0	-164.4
J17524964–2609345	-9.7	0.191	0.407	0.054	-10.0	0.381	1.130	0.066	040420.2	-9.8
J17530105–2548560	-21.5	0.299	1.491	0.038	-15.7	0.248	0.708	0.049	040519.0	-18.6
J17530881–2622009	195.1	0.240	0.468	0.062	200.0	0.166	0.240	0.058	050525.0	197.5
J17532549–2745220	-30.5	0.280	1.334	0.056	-30.4	0.316	0.504	0.068	050525.0	-30.5
J17532550–2753263	-160.8	0.328	1.328	0.058	-161.8	0.306	1.219	0.063	050525.0	-161.3
J17532991–2712445	37.3	0.432	1.687	0.048	35.3	0.343	1.243	0.060	050524.1	36.3
J17540055–2608599	15.4	0.844	3.959	0.054	14.7	0.889	3.282	0.067	040420.2	15.0
J17540931–2556335	41.6	0.176	0.340	0.040	—	—	—	0.049	040519.0	41.6
J17542181–2643520	-118.7	0.254	0.269	0.064	-118.8	0.325	0.713	0.073	040514.1	-118.8
J17545214–2731335	17.3	0.599	1.654	0.064	17.5	0.882	2.642	0.076	050212.4	17.4
J17545809–2727388	264.0	0.279	0.946	0.067	264.9	0.240	0.774	0.072	050212.4	264.5

Table 1. (Continued)

Name	SiO $J = 1-0$ $v = 1$				SiO $J = 1-0$ $v = 2$				Obs. date	V_{ave} (km s $^{-1}$)
	V_{peak} (km s $^{-1}$)	T_{peak} (K)	Flux (K km s $^{-1}$)	RMS (K)	V_{peak} (km s $^{-1}$)	T_{peak} (K)	Flux (K km s $^{-1}$)	RMS (K)		
J17550010–2706132	97.3	0.292	0.614	0.042	96.3	0.202	0.595	0.054	040226.2	96.8

† the MSX position was observed.

Table 2. Negative results.

object name	RMS($v = 1$) (K)	RMS($v = 2$) (K)	Obsdate (yyymmdd.d)
J17352674–3109109	0.060	0.049	40511.0
J17360128–3114433	0.061	0.050	40511.0
J17372673–3132504	0.078	0.059	50527.1
J17375350–3135225	0.079	0.060	50527.1
J17381178–3146270	0.052	0.040	40421.1
J17381803–3053066	0.086	0.073	40421.2
J17382915–3106140	0.047	0.040	40421.1
J17383271–2946546	0.068	0.052	40515.0
J17383832–3120314	0.056	0.042	40515.1
J17383952–3139080	0.067	0.052	40515.1
J17385078–3014244	0.057	0.042	40512.1
J17390880–3024002	0.061	0.053	40419.1
J17391345–3040313	0.055	0.045	40512.1
J17392896–3146120	0.051	0.040	40421.1
J17393560–3153445	0.054	0.042	50212.3
J17394079–3145010	0.053	0.042	40421.1
J17394740–3202224	0.081	0.064	50527.1
J17394900–3043319	0.056	0.046	40512.1
J17395296–3004356	0.071	0.052	50527.0
J17395605–3101564	0.061	0.050	40519.1
J17401510–2936078	0.070	0.052	40422.2
J17403627–2949138	0.069	0.054	50530.0
J17405280–3009137	0.064	0.051	40419.2
J17405979–3142200	0.062	0.048	50524.1
J17410935–3035366	0.051	0.040	50213.3
J17410963–3125595	0.051	0.040	50212.3
J17413156–2958345	0.072	0.055	50530.0
J17413685–2929309	0.049	0.040	50215.3
J17414160–3152426	0.060	0.047	40511.1
J17420381–2920176	0.083	0.060	50529.0
J17421227–2839300	0.056	0.045	50215.4
J17422046–2853213	0.046	0.038	40418.1
J17422144–3005322	0.051	0.067	40419.2
J17423614–3139575	0.063	0.052	40511.1
J17425454–2900470	0.087	0.064	50529.0
J17431105–3033423	0.054	0.044	50310.2
J17432130–2831302	0.061	0.048	50215.4
J17432504–3042281	0.067	0.048	50310.3
J17432861–2904313	0.089	0.066	50529.0
J17432964–2954185	0.064	0.049	50528.1
J17432988–2950074†	0.128	0.090	030513.0
J17434496–2941008	0.072	0.053	50213.3
J17435242–3004275	0.073	0.057	50527.0
J17435946–2930316	0.068	0.053	50528.1
J17441303–2904042	0.116	0.060	50212.4
J17441342–2915408	0.063	0.048	40519.1
J17443710–2948024	0.065	0.049	50528.1
J17444213–2938546	0.072	0.059	50528.1
J17444425–2954215	0.067	0.051	50213.3
J17444503–2804089†	0.102	0.086	040423.2
J17444599–2745088	0.056	0.044	50214.3
J17444741–2948559	0.077	0.056	50528.1
J17444895–2815536	0.092	0.071	40421.1
J17445571–2828070	0.077	0.062	50526.1
J17451006–2953312	0.069	0.052	50213.3

Table 2. (Continued)

object name	RMS($v = 1$) (K)	RMS($v = 2$) (K)	Obsdate (yymmdd.d)
J17451245–2840443	0.070	0.053	40422.1
J17451381–2941498	0.056	0.044	40518.1
J17451446–2814263	0.084	0.064	50526.1
J17451797–3000465	0.068	0.042	50211.3
J17452990–2739169	0.060	0.043	40512.0
J17453565–2807529	0.076	0.062	40511.0
J17454046–3025417	0.051	0.043	40423.1
J17454069–2914544	0.039	0.031	50211.3
J17454656–2832395	0.050	0.038	50211.3
J17454858–3043120	0.091	0.072	50530.1
J17455610–3005401	0.080	0.055	50527.0
J17455681–2728545	0.049	0.039	50213.4
J17461216–2755301	0.075	0.063	50525.1
J17461759–3015515	0.052	0.041	40423.1
J17461787–2936474	0.057	0.043	40518.1
J17462847–2927428	0.060	0.048	40518.1
J17463336–2707577	0.051	0.043	40423.1
J17464524–2815476†	0.115	0.090	030513.2
J17464775–2738140	0.061	0.042	40512.0
J17470666–2756557	0.066	0.053	50525.1
J17472353–2902281	0.064	0.049	50528.0
J17472879–2943392	0.055	0.043	40518.1
J17473979–2610112	0.066	0.048	50528.0
J17474166–2656290	0.052	0.040	40518.0
J17474486–2826365†	0.107	0.078	030513.2
J17474527–2833347	0.046	0.037	40418.2
J17474763–2659030	0.064	0.051	50311.3
J17475612–2943026	0.051	0.043	40518.1
J17482601–2617516	0.065	0.048	50528.0
J17483072–2639334	0.081	0.060	50529.0
J17483328–2825103	0.070	0.055	40511.1
J17484203–2837009	0.086	0.066	50527.1
J17491881–2551060	0.050	0.040	50212.3
J17492553–2710436	0.067	0.055	50311.3
J17492585–2800451	0.101	0.076	40515.1
J17494425–2813284	0.067	0.053	50527.0
J17500176–2635369	0.049	0.039	40225.2
J17501466–2628017	0.138	0.109	50526.0
J17501759–2750147	0.072	0.052	50530.1
J17501892–2842178	0.055	0.046	40419.1
J17502063–2730337	0.076	0.052	50311.2
J17503931–2821079	0.067	0.052	40226.3
J17504797–2822349	0.069	0.053	50527.0
J17504850–2646024	0.078	0.057	40515.0
J17504930–2655505	0.070	0.053	50528.1
J17505341–2616235	0.070	0.051	50310.3
J17505905–2815495	0.069	0.054	50527.0
J17512676–2758379	0.107	0.078	40515.1
J17512808–2726594	0.074	0.057	50311.2
J17513508–2818466	0.067	0.050	40226.3
J17513540–2809594	0.054	0.043	50214.4
J17515225–2722519	0.067	0.053	40226.4
J17521292–2724031	0.075	0.055	50311.2
J17522206–2705429	0.057	0.046	50524.1
J17523535–2719242	0.059	0.046	50524.1

Table 2. (Continued)

object name	RMS($v = 1$) (K)	RMS($v = 2$) (K)	Obsdate (yyymmdd.d)
J17524063–2813437	0.055	0.044	50214.4
J17524471–2616417	0.057	0.045	50210.4
J17524797–2611537	0.059	0.045	50210.4
J17525259–2605193	0.067	0.057	40420.2
J17530019–2808136	0.056	0.043	50214.4
J17530116–2802133	0.067	0.054	50525.0
J17530370–2641590	0.075	0.060	40514.1
J17531860–2555438	0.049	0.036	40519.0
J17531981–2646451	0.074	0.059	40514.1
J17532989–2617515	0.062	0.045	50210.4
J17535485–2627217	0.069	0.056	50525.0
J17540369–2709061	0.055	0.042	40226.2
J17542628–2635178	0.053	0.044	40519.1
J17542897–2734422	0.076	0.058	50212.4
J17544145–2707217	0.054	0.043	40226.2
J17550212–2623550	0.068	0.056	50525.0
J17553626–2642456	0.055	0.045	40519.1
J17555145–2633479	0.053	0.044	40519.1

† : the MSX position was observed.

Table 3. Infrared properties of the observed sources

2MASS name	MSX6C name	Δr_M ($''$)	K (mag)	$J - H$ (mag)	$H - K$ (mag)	F_C (Jy)	C_{CE}	$V_{\text{lsr}}^{\text{SiO}}$ (km s^{-1})	IRAS name	Δr_I ($''$)
J17352480–3058174	G357.1017+00.7945	0.8	8.688	2.855	1.999	2.61	-0.062	-121.5	17321–3056	6.4
J17352674–3109109	G356.9526+00.6906	0.7	8.823	2.864	1.758	2.94	-0.049			
J17354457–3134332	G356.6311+00.4090	0.7	7.734	3.632	2.429	9.57	-0.091	59.8		
J17355075–3057569	G357.1567+00.7196	0.9	8.204	3.314	1.916	2.29	0.001	-270.1	17326–3056	49.1
J17355648–3140399	G356.5680+00.3184	0.7	11.077	0.976	4.417	2.67	-0.138	-169.1	17327–3138	23.3
J17355814–3101029	G357.1272+00.6694	0.8	6.791	2.668	1.632	4.34	-0.162	-65.4		
J17355954–3136317	G356.6319+00.3463	0.4	8.778	3.682	3.200	4.93	0.084	-334.3		
J17360128–3114433	G356.9413+00.5373	1.3	7.820	3.340	1.984	2.28	-0.107		17327–3112	2.6
J17361848–3038053	G357.4890+00.8144	0.7	7.147	2.558	1.493	4.34	-0.147	-98.7	17331–3036	12.1
J17364217–3059117	G357.2381+00.5534	0.1	8.091	4.246	2.333	1.88	0.048	-145.9	17335–3057	21.8
J17371969–3004585	G358.0727+00.9251	0.3	7.471	2.667	1.663	2.80	-0.369	219.3		
J17372673–3132504	G356.8499+00.1188	2.1	7.121	3.850	2.075	2.95	-0.072			
J17373917–2959315	G358.1874+00.9142	1.5	7.058	2.444	1.435	2.39	-0.281	-149.5	17344–2957	12.4
J17374522–3035313	G357.6919+00.5749	1.2	7.009	3.199	1.833	3.63	-0.121	-144.5	17345–3033	7.9
J17374537–3033461	G357.7170+00.5900	0.6	6.768	3.255	1.875	5.86	-0.081	-49.1	17345–3032	27.6
J17375350–3135225	G356.8653+00.0158	1.6	7.087	5.673	2.927	3.04	-0.054		17346–3133	2.4
J17380035–2955522	G358.2799+00.8824	1.4	7.566	2.628	1.795	3.86	-0.081	31.6	17348–2954	22.0
J17380329–3116094	G357.1545+00.1576	1.0	10.993	2.940	4.090	2.55	-0.128	-308.3	17348–3114	4.1
J17380426–3143191	G356.7738–00.0872	1.7	5.633	2.738	1.532	5.84	-0.216	-57.7	17348–3141	2.5
J17381178–3146270	G356.7439–00.1375	2.1	7.017	2.920	1.684	3.39	-0.300		17349–3144	5.5
J17381197–3046271	G357.5892+00.3963	1.4	9.673	2.752	2.459	2.55	-0.208	-63.3		
J17381803–3053066	G357.5070+00.3188	1.8	7.759	3.764	2.203	2.52	0.032		17350–3051	20.4
J17381968–3106094	G357.3264+00.1974	1.4	10.014	3.794	3.990	3.76	0.006	-71.2		
J17382060–3056128	G357.4684+00.2831	0.8	5.566	2.538	1.395	2.43	-0.248	-67.8		
J17382915–3106140	G357.3434+00.1682	1.3	5.072	2.393	1.219	2.76	-0.143			
J17383271–2946546	G358.4684+00.8637	0.8	7.134	3.004	1.914	3.99	-0.139		17353–2945	9.2
J17383569–2936372	G358.6194+00.9459	1.2	8.122	2.776	1.678	1.98	0.039	2.3	17353–2934	14.9
J17383832–3120314	G357.1595+00.0134	1.4	5.950	3.616	1.993	4.79	-0.165		17353–3118	6.0
J17383952–3139080	G356.8995–00.1557	1.7	7.462	3.618	1.919	3.00	-0.197			
J17384240–3153322	G356.7020–00.2925	1.4	8.520	2.737	2.018	3.86	-0.107	-192.1	17354–3151	11.0
J17384424–2926077	G358.7836+01.0131	0.3	8.919	3.188	2.090	3.98	-0.084	96.3	17355–2924	13.8
J17384471–3027057	G357.9249+00.4694	0.5	9.441	3.526	2.735	3.82	0.056	41.3	17354–3025	30.6
J17385078–3014244	G358.1155+00.5637	0.3	8.688	2.849	2.389	1.97	-0.056			
J17385285–3058250	G357.4986+00.1664	1.9	9.686	4.146	4.266	2.60	-0.048	-30.0	17356–3056	9.7
J17385873–3023559	G357.9961+00.4550	1.3	7.478	3.123	1.750	2.30	-0.172	-240.2		
J17390867–3017183	G358.1088+00.4834	1.0	5.036	2.503	1.306	3.75	-0.303	3.7	17359–3015	8.7
J17390880–3024002	G358.0142+00.4240	2.4	7.760	3.268	1.847	2.14	-0.099			
J17391209–2923518	G358.8695+00.9480	1.0	6.027	2.072	1.311	4.46	-0.144	-123.9	17360–2922	2.9
J17391345–3040313	G357.7905+00.2630	1.2	5.796	2.566	1.285	3.27	-0.166		17360–3038	13.7
J17391903–3011097	G358.2154+00.5069	1.5	7.354	2.841	1.947	5.41	-0.126	-147.0	17361–3009	6.9
J17392257–3104456	G357.4657+00.0201	1.9	7.356	4.125	2.117	3.06	-0.198	-194.2		
J17392896–3146120	G356.8933–00.3670	1.5	9.107	2.866	2.127	2.69	-0.045			
J17393560–3153445	G356.7996–00.4538	0.7	7.758	3.421	1.923	3.52	-0.127		17363–3152	10.3
J17394079–3145010	G356.9330–00.3933	5.1	6.079	2.203	1.087	3.86	-0.095		17364–3144	46.6
J17394321–2951276	G358.5398+00.6078	1.1	8.045	2.956	1.762	2.30	-0.024	-204.4		
J17394506–3055582	G357.6326+00.0301	1.4	6.679	2.810	1.685	4.11	-0.173	50.0	17364–3054	43.0
J17394697–3024485	G358.0761+00.3005	1.3	10.165	1.886	4.384	4.49	0.093	-190.7	17365–3023	15.0
J17394740–3202224	G356.6999–00.5656	1.3	8.289	3.155	1.783	2.46	-0.007		17365–3200	33.1
J17394900–3043319	G357.8158+00.1285	1.3	8.051	4.817	2.896	3.17	-0.089		17366–3042	37.7
J17395296–3004356	G358.3730+00.4616	1.5	7.986	3.086	1.911	3.74	-0.202			
J17395605–3101564	G357.5692–00.0559	1.7	8.179	3.965	2.366	3.42	-0.139		17367–3100	3.4
J17395669–2920481	G358.9987+00.8379	0.5	8.221	2.379	2.202	3.65	0.099	82.5	17367–2919	3.6
J17400034–3114314	G357.3995–00.1806	2.2	7.214	3.039	1.816	2.21	-0.321	77.3	17367–3112	17.2
J17400912–2959191	G358.4786+00.4588	0.7	9.052	2.504	1.819	2.25	-0.033	114.2		
J17401355–2956426	G358.5239+00.4684	1.1	6.038	2.349	1.246	2.13	-0.130	-159.6		

Table 3. (Continued)

2MASS name	MSX6C name	Δr_M ($''$)	K (mag)	$J - H$ (mag)	$H - K$ (mag)	F_C (Jy)	C_{CE}	V_{lsr}^{SiO} (km s^{-1})	IRAS name	Δr_I ($''$)
J17401510–2936078	G358.8174+00.6455	0.9	8.909	3.206	2.035	2.34	0.015		17370–2934	7.5
J17401688–3032596	G358.0174+00.1374	2.8	8.891	4.268	2.757	4.05	-0.156	-219.9	17370–3031	3.6
J17402241–3027273	G358.1065+00.1692	1.2	6.557	2.890	1.561	3.63	-0.132	-318.7	17371–3025	8.7
J17403247–2846360	G359.5512+01.0298	0.7	6.586	2.490	1.407	2.70	-0.162	-88.0	17373–2845	9.2
J17403627–2949138	G358.6731+00.4649	0.8	7.894	2.079	1.187	1.56	0.093			
J17403670–2933111	G358.9002+00.6066	5.4	8.409	2.239	2.420	2.45	-0.097	-186.3	17373–2931	40.6
J17403750–2904098	G359.3124+00.8594	1.1	6.884	3.122	1.805	1.78	0.090	79.2	17374–2902	8.6
J17404146–3132304	G357.2234–00.4637	1.2	7.910	3.403	2.195	3.28	-0.025	-166.5	17374–3131	9.3
J17404825–3050360	G357.8286–00.1137	1.1	8.748	4.229	2.727	2.49	-0.052	-84.5		
J17404953–3055183	G357.7643–00.1591	1.7	6.757	3.280	1.929	2.43	-0.079	-85.8	17375–3053	54.0
J17405280–3009137	G358.4218+00.2379	2.0	6.972	2.325	1.251	5.87	0.100		17376–3007	3.8
J17405431–3144125	G357.0820–00.6057	1.8	6.746	2.730	1.627	3.47	-0.049	-42.2	17376–3142	2.3
J17405979–3142200	G357.1195–00.6066	4.1	9.707	1.747	2.808	2.74	0.123		17377–3140	3.3
J17410791–3159544	G356.8857–00.7851	1.3	8.663	3.773	2.355	3.42	-0.058	174.5	17378–3158	5.4
J17410935–3035366	G358.0808–00.0452	1.6	6.382	3.895	2.060	5.51	-0.259		17379–3034	8.3
J17410963–3125595	G357.3684–00.4909	1.5	6.776	2.284	1.148	3.41	-0.154		17379–3124	5.7
J17411056–3008096	G358.4710+00.1928	1.0	7.548	4.198	2.500	4.57	-0.067	-127.1		
J17411421–2851112	G359.5669+00.8601	0.1	7.258	2.475	1.549	1.47	0.121	-5.4	17380–2849	11.6
J17411489–3000159	G358.5908+00.2491	1.5	8.742	3.152	1.921	2.37	-0.102	68.2		
J17411834–3002290	G358.5659+00.2193	2.1	8.680	3.540	2.555	3.09	-0.169	15.8	17380–3001	10.5
J17413156–2958345	G358.6464+00.2133	2.2	8.172	3.590	2.119	1.79	-0.019			
J17413541–2854274	G359.5616+00.7656	0.4	9.090	2.990	2.123	2.88	-0.038	128.4	17384–2853	25.6
J17413685–2929309	G359.0679+00.4525	1.1	7.581	3.154	1.950	2.89	-0.097			
J17413828–3145337	G357.1454–00.7499	1.6	5.137	2.637	1.597	12.74	-0.091	21.1	17383–3144	3.1
J17414160–3152426	G357.0505–00.8226	0.8	10.148	3.269	2.705	2.42	-0.126		17384–3151	8.5
J17414205–3132063	G357.3426–00.6429	2.6	10.310	1.196	3.539	3.51	0.026	59.2	17384–3130	27.2
J17414293–3158231	G356.9727–00.8767	0.8	8.683	3.443	2.197	2.20	-0.076	-145.4	17384–3156	25.7
J17420381–2920176	G359.2500+00.4507	1.5	9.440	3.308	3.616	2.93	-0.043			
J17420881–2955044	G358.7668+00.1298	2.9	9.764	2.254	2.854	2.93	0.004	-95.0	17388–2953	52.4
J17421172–3057189	G357.8913–00.4263	0.9	7.412	3.674	1.859	4.51	-0.107	-6.9	17389–3055	6.2
J17421227–2839300	G359.8444+00.7829	0.2	7.495	2.971	1.673	3.23	-0.140		17390–2838	17.0
J17421783–2936334	G359.0467+00.2644	0.8	8.629	3.354	2.412	1.33	0.017	-159.6		
J17421887–3015288	G358.4970–00.0801	2.7	5.156	2.707	1.567	14.87	-0.109	-24.2	17390–3014	26.7
J17422046–2853213	G359.6638+00.6358	0.2	10.312	3.440	2.919	2.27	0.068			
J17422144–3005322	G358.6428–00.0009	2.0	8.579	4.301	2.483	2.96	-0.105			
J17422438–3135073	G357.3793–00.7972	2.3	10.062	3.101	3.521	2.66	0.047	-107.1	17391–3133	6.0
J17423614–3139575	G357.3331–00.8751	1.7	10.458	2.555	4.299	4.07	-0.021		17393–3138	5.8
J17424091–3015134	G358.5424–00.1455	2.5	7.662	4.154	2.573	4.47	-0.022	-82.7		
J17424480–2932464	G359.1515+00.2148	1.8	11.105	2.331	3.227	2.27	0.121	-35.3		
J17425115–2951513†	G358.8932+00.0277	3.8	4.913	3.419	1.834	27.17	-0.188	-13.3		
J17425454–2900470	G359.6241+00.4652	0.7	8.937	4.044	2.345	1.75	-0.147			
J17425616–2931498	G359.1863+00.1880	2.6	9.015	3.762	2.557	2.85	-0.172	-138.3		
J17425698–2910005	G359.4979+00.3767	0.4	8.144	4.110	2.260	1.88	-0.132	-20.2		
J17425995–2957026	G358.8361–00.0445	2.8	7.154	4.444	2.413	9.56	-0.061	-115.9		
J17430330–2938016	G359.1122+00.1117	2.3	9.450	2.640	2.874	2.94	-0.012	-52.1	17398–2936	23.0
J17430552–3018014	G358.5493–00.2454	2.1	6.754	4.119	2.404	12.93	-0.078	-17.4	17398–3016	4.2
J17430981–2924033	G359.3228+00.2140	1.8	8.193	4.757	2.594	3.78	-0.038	-55.2		
J17431105–3033423	G358.3375–00.3997	1.9	8.666	2.955	3.144	3.32	-0.109		17399–3032	3.7
J17431231–2928496	G359.2596+00.1645	2.7	9.511	4.164	4.293	5.42	0.014	75.5	17400–2927	10.4
J17432130–2831302	G000.0904+00.6383	0.7	9.498	2.272	2.629	2.34	0.027		17401–2830	5.4
J17432504–3042281	G358.2398–00.5195	1.1	9.224	3.695	2.589	2.41	-0.238			
J17432861–2904313	G359.6365+00.3267	1.0	8.934	3.792	2.222	1.55	-0.171			
J17432963–2804137	G000.4941+00.8508	1.9	8.513	3.080	2.170	2.61	-0.017	303.5		
J17432964–2954185	G358.9314–00.1116	2.3	10.035	3.581	3.653	1.68	-0.147		17403–2953	53.2
J17432988–2950074†	G358.9913–00.0758	3.4	8.823	4.975	3.741	25.50	-0.246		17403–2948	21.7

Table 3. (Continued)

2MASS name	MSX6C name	Δr_M ($''$)	K (mag)	$J - H$ (mag)	$H - K$ (mag)	F_C (Jy)	C_{CE}	$V_{\text{lsr}}^{\text{SiO}}$ (km s^{-1})	IRAS name	Δr_I ($''$)
J17433271–2915393	G359.4858+00.2165	0.7	7.474	3.703	2.158	2.65	-0.220	-94.2		
J17433894–2814165	G000.3690+00.7339	0.2	9.907	2.001	3.183	2.61	0.136	120.1	17404–2813	3.2
J17434496–2941008	G359.1490–00.0426	2.3	5.829	3.666	2.019	26.07	0.237		17405–2939	11.6
J17435079–2845203	G359.9509+00.4254	0.3	8.436	3.958	2.363	2.71	-0.108	-146.8		
J17435211–3057289	G358.0775–00.7332	1.3	8.915	4.128	2.636	3.03	0.003	-38.5	17406–3056	4.9
J17435242–3004275	G358.8304–00.2706	2.4	9.936	2.217	3.208	2.75	0.065			
J17435366–2755443	G000.6604+00.8499	0.4	8.111	2.718	1.915	4.20	-0.064	-142.5	17407–2754	4.4
J17435898–2743109	G000.8491+00.9427	0.4	6.244	2.142	1.178	2.61	-0.271	-40.1	17407–2741	34.8
J17435946–2930316	G359.3258+00.0040	0.9	9.415	3.505	2.903	0.92	0.208		17407–2928	27.9
J17440282–2740425	G000.8917+00.9523	0.7	9.174	3.646	2.808	5.21	0.031	126.1	17408–2739	1.8
J17440469–2919538	G359.4865+00.0806	1.0	9.583	3.426	3.856	3.17	-0.099	-48.4		
J17440744–2927376†	G359.3819+00.0049	2.6	6.534	4.876	2.615	10.81	-0.245	-204.4	17409–2926	5.6
J17441303–2904042	G359.7273+00.1928	0.7	9.012	4.038	2.347	2.71	-0.091			
J17441342–2915408	G359.5636+00.0905	1.2	8.873	4.284	2.486	1.28	-0.120			
J17441431–2821234	G000.3358+00.5602	4.0	7.473	2.627	1.473	4.00	-0.040	-181.4		
J17441640–3039103	G358.3829–00.6472	1.4	7.983	3.664	2.046	2.32	-0.192	-172.8		
J17441922–2844217	G000.0192+00.3456	0.6	8.732	4.290	3.084	3.83	0.113	16.2	17411–2843	30.6
J17443085–2950132	G359.1053–00.2647	1.8	7.895	2.730	1.486	1.06	---	-123.1		
J17443262–2856120	G359.8764+00.2006	0.5	7.911	6.520	3.255	4.26	-0.002	-68.7		
J17443496–2904356†	G359.7616+00.1204	3.0	9.236	2.557	3.787	16.46	0.059	-5.5	17413–2903	27.0
J17443502–3034437	G358.4808–00.6652	1.9	7.596	4.078	2.341	3.24	-0.184	-96.3		
J17443710–2948024	G359.1487–00.2658	3.3	9.357	4.621	3.173	1.74	-0.037			
J17444213–2938546	G359.2871–00.2009	2.6	11.070	2.055	3.355	1.43	0.074			
J1744425–2954215	G359.0719–00.3420	1.4	5.720	2.759	1.396	6.03	-0.215		17415–2953	15.3
J17444503–2804089†	G000.6398+00.6155	0.1	2.936	1.107	0.363	4.78	-0.486		17415–2803	10.3
J17444599–2745088†	G000.9119+00.7780	0.5	7.928	3.207	1.980	2.85	-0.231			
J17444741–2948559	G359.1550–00.3045	1.5	8.804	5.336	2.861	2.01	0.004		17416–2947	37.6
J17444895–2815536	G000.4805+00.5010	0.6	8.674	3.424	2.315	1.90	-0.023			
J17444943–2757017	G000.7486+00.6641	3.9	9.357	2.489	2.331	3.27	0.019	-149.0	17416–2755	43.8
J17445129–2924548†	G359.5035–00.1073	4.7	4.737	3.759	1.999	26.68	-0.210	-60.7		
J17445365–2812464	G000.5338+00.5134	0.1	7.260	3.481	1.855	4.81	-0.083	-79.2	17417–2811	6.0
J17445521–2819209	G000.4431+00.4511	1.2	6.978	2.770	1.741	3.94	-0.124	-139.1		
J17445571–2828070	G000.3198+00.3732	0.6	9.469	3.833	2.297	1.85	-0.072			
J17445788–2957209	G359.0552–00.4097	1.6	6.922	3.430	1.961	2.75	-0.113	-198.0	17417–2956	19.6
J17445891–3021064	G358.7194–00.6197	1.6	7.419	4.725	2.880	4.74	-0.026	-40.0	17417–3019	2.0
J17451006–2953312	G359.1328–00.4143	0.3	9.851	2.011	3.062	2.03	-0.093		17419–2952	6.7
J17451245–2840443	G000.1721+00.2111	0.8	9.798	2.796	2.628	3.36	0.032			
J17451381–2941498	G359.3057–00.3240	2.1	8.441	4.212	2.506	1.54	-0.053			
J17451393–2915279	G359.6808–00.0951	2.1	9.918	3.692	2.306	3.81	0.232	-101.7		
J17451446–2814263	G000.5502+00.4335	0.9	9.189	2.479	2.516	2.08	0.035			
J17451797–3000465	G359.0443–00.5015	1.3	9.127	3.673	2.824	2.94	-0.159		17420–2959	11.1
J17452990–2739169	G001.0799+00.6908	0.8	8.478	3.820	2.386	2.22	-0.065		17423–2738	12.5
J17453430–2747330	G000.9704+00.6051	0.8	9.641	1.639	3.335	4.76	-0.048	-50.2	17424–2746	11.0
J17453506–2822467	G000.4707+00.2967	0.6	8.078	4.209	2.868	10.47	-0.038	-54.2	17424–2821	9.9
J17453565–2807529	G000.6836+00.4244	1.2	6.346	2.963	1.809	5.19	-0.085		17424–2806	5.0
J17454037–2801085	G000.7885+00.4680	1.2	8.951	3.521	2.169	1.10	-0.005	-132.1		
J17454046–3025417	G358.7320–00.7869	1.9	8.409	2.843	2.583	2.89	-0.303			
J17454069–2914544	G359.7396–00.1727	3.0	10.621	4.324	2.431	2.41	-0.088			
J17454130–2746484	G000.9943+00.5895	0.9	8.009	3.395	1.924	3.00	-0.311	-24.4		
J17454184–2657317	G001.6966+01.0161	2.4	10.057	1.610	2.569	4.21	0.107	-3.7	17425–2656	7.0
J17454390–2825200	G000.4512+00.2471	1.0	10.147	3.481	4.037	2.16	-0.085	83.6		
J17454656–2832395	G000.3520+00.1748	1.0	10.346	3.139	3.489	2.66	-0.029			
J17454858–3043120	G358.4983–00.9642	0.8	9.972	2.090	3.271	2.61	0.125		17426–3042	49.3
J17454949–2933293	G359.4917–00.3618	2.0	8.884	3.628	2.563	1.20	-0.112	56.6		
J17455608–2839274	G000.2733+00.0862	1.2	9.790	3.915	3.282	3.89	-0.121	105.4		

Table 3. (Continued)

2MASS name	MSX6C name	Δr_M ($''$)	K (mag)	$J - H$ (mag)	$H - K$ (mag)	F_C (Jy)	C_{CE}	V_{lsr}^{SiO} (km s^{-1})	IRAS name	Δr_I ($''$)
J17455610–3005401	G359.0464–00.6616	1.2	9.606	4.328	2.836	2.12	-0.055		17427–3004	17.4
J17455681–2728545	G001.2790+00.6962	1.1	7.788	2.837	1.825	2.09	0.019		17427–2727	5.6
J17455842–2925319	G359.6217–00.3199	3.2	6.877	4.479	2.400	2.63	-0.207	-101.7		
J17460233–2803339	G000.7959+00.3782	1.7	5.171	2.146	1.226	3.77	-0.118	-2.8	17428–2802	4.3
J17461216–2755301	G000.9296+00.4171	1.3	8.623	3.189	1.903	1.95	—			
J17461759–3015515	G358.9420–00.8157	1.0	10.573	3.776	3.062	2.28	-0.104		17430–3014	5.2
J17461787–2936474	G359.4983–00.4782	1.7	9.398	1.559	3.465	1.74	0.014			
J17462676–2800037	G000.8928+00.3318	1.3	6.971	3.786	2.008	1.65	0.102	33.1		
J17462847–2927428	G359.6494–00.4335	6.0	8.512	3.123	1.500	4.93	0.083		17433–2926	19.6
J17463336–2707577	G001.6476+00.7618	0.6	8.500	3.535	2.481	3.14	-0.032		17434–2706	3.8
J17464524–2815476†	G000.7036+00.1375	1.4	7.184	5.430	2.776	22.94	-0.439		17435–2814	5.1
J17464775–2738140	G001.2441+00.4544	0.5	5.268	2.551	1.288	3.14	-0.226		17436–2737	19.5
J17465135–2917251	G359.8376–00.4143	0.8	10.286	4.088	3.497	1.81	-0.001	-56.0		
J17465644–2726132	G001.4319+00.5310	0.9	7.846	3.770	2.691	2.59	-0.052	-67.5	17437–2725	2.6
J17465905–2817037	G000.7123+00.0841	4.0	11.193	1.406	1.715	3.23	0.040	98.4		
J17465960–2706131	G001.7228+00.6937	1.2	6.812	3.599	2.361	9.59	-0.014	-122.5	17438–2705	6.1
J17470149–2755168	G001.0270+00.2636	1.8	8.483	4.614	2.709	2.99	-0.314	141.4		
J17470666–2756557	G001.0134+00.2333	1.3	8.423	4.219	2.417	2.15	-0.195			
J17471226–2652362	G001.9414+00.7711	0.3	8.720	2.107	2.816	2.61	-0.005	22.4	17440–2651	7.0
J17471986–2837345	G000.4592–00.1587	2.1	11.480	2.707	3.503	1.59	-0.029	-172.7		
J17472353–2902281	G000.1111–00.3850	2.3	5.106	2.562	1.454	4.59	-0.404			
J17472879–2943392	G359.5336–00.7573	1.8	9.078	2.184	2.657	0.97	0.084		17442–2942	1.8
J17473221–2807030	G000.9178+00.0659	2.2	9.965	2.258	3.564	1.44	-0.014	-214.7		
J17473739–2743116	G001.2680+00.2550	1.0	5.215	2.584	1.494	2.30	-0.185	-36.7		
J17473906–2818282	G000.7680–00.0545	1.2	9.538	2.989	3.545	1.83	-0.037	-276.5		
J17473979–2610112	G002.5994+01.0491	0.5	9.548	2.733	2.325	2.31	-0.185		17445–2609	10.8
J17474166–2656290	G001.9421+00.6440	2.0	8.804	2.372	1.667	2.02	0.076		17445–2655	25.4
J17474486–2826365†	G000.6626–00.1428	3.7	10.284	3.370	3.935	14.79	-0.221			
J17474527–2833347	G000.5644–00.2038	2.0	8.457	4.054	3.172	3.47	-0.076			
J17474763–2659030	G001.9170+00.6030	1.9	8.483	2.529	1.688	3.62	-0.136		17446–2658	8.3
J17475612–2943026	G359.5937–00.8366	0.9	8.594	3.132	2.613	3.28	0.017		17447–2942	20.1
J17481087–2920527	G359.9376–00.6914	1.0	5.149	2.072	1.256	6.26	-0.160	8.6	17450–2919	17.1
J17481382–2725523	G001.5844+00.2889	2.0	5.288	2.592	1.863	44.82	-0.031	-29.5	17450–2724	7.3
J17481674–2836124	G000.5859–00.3251	2.7	10.052	1.479	3.127	2.70	-0.160	-30.8		
J17482601–2617516	G002.5792+00.8352	0.3	6.703	2.356	1.397	3.12	-0.045		17453–2616	8.9
J17482755–2829176	G000.7051–00.2996	2.3	8.538	3.279	3.117	3.40	-0.129	-145.1	17452–2828	0.8
J17482827–2810434	G000.9718–00.1422	2.0	7.824	5.144	2.918	3.04	-0.098	-186.1		
J17483072–2639334	G002.2783+00.6338	1.4	8.040	2.190	1.522	2.47	-0.154		17453–2638	4.9
J17483260–2630193	G002.4142+00.7073	1.5	9.440	1.678	2.165	4.02	-0.051	-173.7	17454–2629	37.1
J17483328–2825103	G000.7755–00.2827	1.1	9.345	2.937	2.570	2.94	-0.030		17453–2824	20.2
J17483491–2705072	G001.9208+00.4006	2.7	7.554	2.880	1.723	2.62	-0.116	-213.8	17454–2704	2.4
J17483707–2622249	G002.5355+00.7607	0.6	5.970	2.378	1.420	5.28	-0.219	-108.5	17455–2621	1.7
J17484102–2749458	G001.2954–00.0022	1.3	9.434	3.011	4.742	4.64	-0.066	-139.0		
J17484203–2837009	G000.6223–00.4117	1.7	8.976	4.056	2.487	1.43	-0.016			
J17484246–2737518	G001.4678+00.0954	2.3	7.715	3.758	2.210	1.19	0.120	135.4		
J17484466–2714523	G001.8004+00.2857	1.5	9.411	3.138	2.957	3.22	-0.089	-125.7		
J17484743–2629591	G002.4474+00.6626	0.7	6.600	2.097	1.313	2.11	—	40.4		
J17485495–2635343	G002.3818+00.5906	0.8	8.456	3.976	2.823	5.68	0.035	95.7	17457–2634	15.8
J17485855–2858392	G000.3441–00.6492	2.4	6.652	3.059	1.688	2.17	-0.086	72.2		
J17490836–2733293	G001.5795+00.0508	2.1	6.581	3.104	1.806	4.18	-0.059	-114.8	17460–2732	6.0
J17491881–2551060	G003.0635+00.8955	0.5	6.797	1.714	0.841	2.38	-0.066		17462–2550	5.2
J17492553–2710436	G001.9371+00.1914	3.5	8.521	3.759	2.351	2.77	-0.020			
J17492585–2800451	G001.2237–00.2383	0.1	7.761	3.633	1.909	2.02	-0.086		17462–2759	8.3
J17493449–2633320	G002.4868+00.4816	0.4	8.773	2.638	2.311	4.54	0.037	-45.8	17464–2632	4.2
J17494425–2813284	G001.0762–00.4051	1.5	5.568	1.175	0.532	1.31	0.368		17466–2812	23.2

Table 3. (Continued)

2MASS name	MSX6C name	Δr_M ($''$)	K (mag)	$J - H$ (mag)	$H - K$ (mag)	F_C (Jy)	C_{CE}	$V_{\text{lsr}}^{\text{SiO}}$ (km s^{-1})	IRAS name	Δr_I ($''$)
J17494622–2857454	G000.4456–00.7924	8.3	6.879	2.553	1.702	3.40	0.002	188.0	17466–2856	19.0
J17494935–2906177	G000.3304–00.8737	1.4	7.992	2.588	1.577	3.00	-0.096	57.2	17466–2905	5.1
J17495130–2700444	G002.1297+00.1950	1.2	10.208	1.435	2.766	5.75	-0.015	-163.7	17467–2659	4.1
J17500176–2635369	G002.5093+00.3767	0.8	6.509	2.848	1.537	2.75	-0.271		17469–2634	8.4
J17501466–2628017	G002.6422+00.4003	1.3	5.019	2.082	1.056	2.70	-0.024			
J17501702–2845426	G000.6761–00.7837	3.3	7.865	2.167	1.214	6.36	0.037	25.7	17471–2844	3.4
J17501759–2750147	G001.4710–00.3115	2.8	9.220	3.278	2.401	1.78	-0.095			
J17501892–2842178	G000.7289–00.7603	2.4	8.376	2.962	1.902	2.38	-0.185			
J17502063–2730337	G001.7587–00.1529	1.8	9.684	4.063	3.154	2.32	-0.043		17472–2729	12.7
J17502615–2647048	G002.3917+00.2008	0.8	5.734	2.523	1.376	2.97	-0.190	-92.3	17473–2646	34.7
J17502764–2818388	G001.0838–00.5860	1.9	5.608	2.408	1.417	5.22	-0.170	-108.9	17472–2817	4.5
J17502871–2843472	G000.7258–00.8041	2.0	7.352	2.847	1.743	2.04	-0.135	276.3	17472–2842	37.6
J17502910–2550299	G003.2072+00.6744	0.3	8.848	2.395	1.756	7.77	0.089	-60.4	17473–2549	3.8
J17503133–2803362	G001.3062–00.4690	1.7	9.885	1.869	2.380	3.40	-0.108	129.6		
J17503382–2622283	G002.7588+00.3863	0.6	8.194	3.202	1.734	1.93	0.174	-52.0	17473–2621	57.2
J17503931–2821079	G001.0704–00.6439	1.2	8.228	2.432	1.468	1.62	-0.071			
J17504394–2840427	G000.7988–00.8257	0.4	7.965	2.610	1.529	2.51	-0.102	96.1	17475–2839	11.3
J17504797–2822349	G001.0659–00.6836	1.2	8.111	2.621	1.766	1.93	0.090		17476–2821	5.8
J17504850–2646024	G002.4506+00.1379	4.5	9.027	3.757	1.835	0.86	0.477		17476–2645	10.6
J17504930–2655505	G002.3103+00.0520	1.0	10.874	3.015	4.467	2.43	-0.018			
J17505341–2616235	G002.8832+00.3753	0.1	7.995	3.787	2.174	2.82	-0.059		17477–2615	23.7
J17505365–2556283	G003.1688+00.5444	0.1	7.609	2.778	1.566	2.16	-0.214	-36.2	17477–2555	4.1
J17505401–2709177	G002.1266–00.0775	1.4	6.488	3.372	1.954	4.46	-0.131	7.9	17478–2708	38.7
J17505784–2625025	G002.7676+00.2880	2.6	7.096	3.501	2.047	1.74	-0.057	-106.4	17478–2624	5.8
J17505905–2815495	G001.1835–00.6611	0.7	7.419	2.302	1.433	1.81	-0.096		17478–2815	2.8
J17510037–2640020	G002.5578+00.1514	0.8	9.957	1.608	2.667	2.41	-0.044	-57.8		
J17510408–2718506	G002.0083–00.1913	3.3	7.595	3.608	2.679	2.39	-0.205	21.6		
J17512676–2758379	G001.4812–00.6020	2.9	7.553	2.360	1.460	2.77	-0.152		17482–2758	11.1
J17512808–2726594	G001.9371–00.3370	2.7	8.135	2.273	3.134	7.29	0.049		17483–2726	17.7
J17513508–2818466	G001.2086–00.7998	1.2	8.759	1.927	2.094	3.64	-0.022		17484–2818	1.2
J17513540–2809594	G001.3351–00.7254	2.9	10.390	1.341	2.648	3.45	-0.124		17484–2809	14.9
J17514250–2709204	G002.2174–00.2336	4.0	8.210	2.811	1.550	1.90	-0.041	47.6		
J17514587–2635481	G002.7048+00.0417	1.3	8.098	3.588	2.322	6.85	-0.060	-56.3	17486–2635	33.6
J17515225–2722519	G002.0422–00.3786	1.7	9.818	2.454	3.126	3.25	-0.123		17487–2722	44.3
J17520753–2628180	G002.8535+00.0367	2.5	7.008	2.963	1.748	4.03	0.050	16.0	17489–2627	37.8
J17520868–2711412	G002.2335–00.3360	1.6	5.977	3.315	2.015	15.07	-0.056	-81.5	17490–2711	5.7
J17521292–2724031	G002.0643–00.4543	1.5	9.631	1.796	2.188	2.08	0.029		17491–2723	20.9
J17522130–2720043	G002.1360–00.4491	8.2	8.057	2.986	1.702	2.41	-0.159	273.6		
J17522206–2705429	G002.3447–00.3281	0.6	9.282	2.294	3.159	5.23	-0.125		17492–2705	4.5
J17523535–2719242	G002.1731–00.4865	1.4	9.079	4.494	2.732	2.15	-0.033			
J17524063–2813437	G001.4031–00.9637	3.0	5.589	1.583	1.289	14.74	-0.068		17495–2813	10.7
J17524471–2616417	G003.0909+00.0151	0.6	6.568	3.190	1.761	3.89	-0.205		17496–2616	14.7
J17524797–2611537	G003.1659+00.0452	0.9	5.480	2.030	1.193	3.50	-0.195		17496–2611	4.9
J17524903–2607386	G003.2289+00.0778	1.1	7.789	3.493	2.082	4.64	-0.170	-164.4	17497–2607	5.4
J17524964–2609345	G003.2022+00.0592	1.9	8.611	4.608	2.929	5.67	-0.087	-9.8	17497–2608	8.5
J17525259–2605193	G003.2689+00.0860	1.1	8.881	2.761	2.101	2.63	-0.090		17497–2604	4.4
J17530019–2808136	G001.5187–00.9789	2.9	7.248	2.275	1.256	2.74	-0.057		17498–2807	1.3
J17530105–2548560	G003.5205+00.1978	0.6	6.447	2.491	1.461	2.24	0.142	-18.6	17499–2548	19.8
J17530116–2802133	G001.6066–00.9311	3.1	8.098	2.996	1.783	2.37	-0.143		17498–2801	22.2
J17530370–2641590	G002.7640–00.2599	0.7	9.005	4.639	2.699	2.11	0.078		17499–2641	31.9
J17530881–2622009	G003.0602–00.1073	1.0	6.779	2.735	1.566	3.86	-0.208	197.5	17500–2621	32.2
J17531860–2555438	G003.4565+00.0836	0.6	8.052	1.109	2.481	2.63	-0.099			
J17531981–2646451	G002.7261–00.3518	1.3	9.140	2.639	2.613	3.26	0.013			
J17532549–2745220	G001.8941–00.8657	3.3	6.509	2.370	1.463	6.49	-0.134	-30.5	17503–2744	55.1
J17532550–2753263	G001.7781–00.9337	4.0	9.022	2.406	2.790	2.41	0.020	-161.3	17502–2752	2.1

Table 3. (Continued)

2MASS name	MSX6C name	Δr_M ($''$)	K (mag)	$J - H$ (mag)	$H - K$ (mag)	F_C (Jy)	C_{CE}	V_{lsr}^{SiO} (km s^{-1})	IRAS name	Δr_I ($''$)
J17532989–2617515	G003.1599–00.1401	0.7	8.025	3.893	2.271	3.30	-0.187		17503–2617	5.7
J17532991–2712445	G002.3716–00.6042	1.1	8.877	4.361	2.761	2.36	-0.251	36.3		
J17535485–2627217	G003.0703–00.3002	2.6	6.998	3.743	1.818	2.51	-0.096		17508–2626	2.3
J17540055–2608599	G003.3453–00.1641	0.9	8.285	3.173	2.933	5.98	-0.033	15.0	17509–2608	4.3
J17540369–2709061	G002.4873–00.6812	1.7	8.623	3.835	2.622	2.95	-0.190			
J17540931–2556335	G003.5410–00.0870	1.3	8.618	4.004	2.224	2.65	-0.174	41.6	17510–2555	22.3
J17542181–2643520	G002.8845–00.5265	0.5	10.236	4.716	2.627	3.14	0.075	-118.8		
J17542628–2635178	G003.0156–00.4685	1.7	8.439	3.423	2.220	3.56	-0.002		17513–2634	26.0
J17542897–2734422	G002.1664–00.9779	2.0	8.017	2.727	1.621	2.35	-0.037		17513–2734	18.5
J17544145–2707217	G002.5837–00.7879	1.6	7.851	3.192	1.891	2.25	-0.149			
J17545214–2731335	G002.2552–01.0260	2.1	5.959	2.717	1.767	10.53	0.011	17.4	17517–2731	2.2
J17545809–2727388	G002.3227–01.0118	1.4	8.523	2.692	1.788	2.87	0.031	264.5	17518–2727	13.4
J17550010–2706132	G002.6345–00.8374	1.3	9.260	1.195	2.859	3.69	-0.050	96.8	17518–2705	1.9
J17550212–2623550	G003.2467–00.4881	2.0	7.770	3.137	1.845	2.28	-0.085		17518–2623	18.7
J17553626–2642456	G003.0400–00.7559	2.2	10.375	3.107	3.390	2.66	0.145		17524–2642	46.5
J17555145–2633479	G003.1975–00.7299	1.4	7.746	3.348	1.955	1.84	-0.043			

† : the MSX position was observed.

Table 4. Previously observed sources (detected in Deguchi et al. 2000).

2MASS name	MSX6C name	Δr_M (")	K (mag)	$J - H$ (mag)	$H - K$ (mag)	F_C (Jy)	C_{CE}	$V_{\text{lsr}}^{\text{SiO}}$ (km s $^{-1}$)	IRAS name	Δr_I (")
J17371631–3131192	G356.8515+00.1635	1.8	8.266	6.134	3.704	8.24	-0.139	-85.9	17340–3129	25.7
J17391263–3044163	G357.7361+00.2321	0.9	6.645	3.836	2.246	5.72	-0.105	—	17359–3042	2.7
J17404994–2946001	G358.7448+00.4516	1.3	8.650	3.826	2.347	3.21	-0.007	0.3	17376–2944	2.4
J17431499–2853280	G359.7669+00.4658	0.6	7.359	3.640	1.974	2.21	-0.180	— ^b	17400–2852	17.7
J17494019–2844464	G000.6207–00.6604	2.5	10.147	1.809	4.832	11.81	-0.071	-46.2	17464–2843	16.0
J17512677–2825371	G001.0950–00.8316	1.5	5.973 [#]	3.615	-0.339 [#]	157.50	0.124	10.3	17482–2824	2.3
J17512732–2614202	G002.9775+00.2838	0.6	9.080	5.712	2.965	2.66	-0.113	163.2	17483–2613	6.3
J17554427–2627458	G003.2709–00.6565	1.4	8.650	0.734	2.697	2.32	0.188	-42.8	17526–2627	4.9

^b Nondetection by Messineo et al. (2003).[#] Star image severely blended in the K band.Table 5. Previous OH and H₂O detections

2MASS name	OH/H ₂ O name	Δr (")	$V_{\text{lsr}}^{\text{OH/H}_2\text{O}}$ (km s $^{-1}$)	$V_{\text{lsr}}^{\text{SiO}}$ (km s $^{-1}$)	reference
J17354457–3134332	OH 356.631+00.409	0.5	59.7	59.8	(1)
J17404953–3055183	OH 357.77–00.15(?)	37.3	-80.0	-85.8	(2)
J17405280–3009137	OH 358.422+00.238	0.4	122(S)	—	(1)
J17413828–3145337	OH 357.146–00.750	0.2	21.1	21.1	(1)
J17421887–3015288	OH 358.497–00.081	0.7	-22.0	-24.2	(1)
J17422046–2853213	OH 359.664+00.636	1.0	-160.0	—	(1)
J17431231–2928496	H ₂ O 359.260+00.164	0.7	54.8	75.5	(3)
J17434496–2941008	OH 359.149–00.043	1.3	37.1	—	(1)
J17445891–3021064	OH 358.720–00.620	0.4	-20.6(S)	-40.0	(1)
J17451381–2941498	OH 359.681–0.095	6.3	-98.7	—	(4)
J17483328–2825103	OH 000.775–00.282	0.7	192(S)	—	(1)
J17485495–2635343	OH 002.382+00.590	0.1	94.8	95.7	(1)
J17502910–2550299	OH 003.207+00.675	0.6	-60.7	-60.4	(1)
J17531981–2646451	OH 002.726–00.352	0.7	-143.2	—	(1)

reference: (1) Sevenster et al. (1997), (2) Caswell et al. (1981),

(3) Taylor et al. (1993), (4) Sjouwerman et al. (1998)

Table 6. Results of statistical analysis for the eccentric velocity sets

Set	group	number	K_{H-K}^{ave}	stand.dev.	t-probability
Present SiO sample	$V_{\text{lsr}} < 0$	15	5.727	0.881	0.43
	$V_{\text{lsr}} > 0$	7	5.975	0.547	
added IRAS/SiO objects (within $ l < 3^\circ$ and $ l < 3^\circ$)	$V_{\text{lsr}} < 0$	19	5.871	1.009	0.34
	$V_{\text{lsr}} < 0$	12	6.197	0.839	
added OH 1612 MHz objects (within $ l < 3^\circ$ and $ l < 3^\circ$)	$V_{\text{lsr}} < 0$	27	6.432	1.662	0.32
	$V_{\text{lsr}} > 0$	19	6.914	1.571	

Table 7. Statistics for the supposed x_1 and x_2 family sets within $|l| < 1.5^\circ$ and $|V_{\text{lsr}}| < 150$ km s $^{-1}$.

Set	quantity	number	mean	stand.dev.	t-probability
supposed x_1 family set	$ b $	27	0.527	0.267	0.10
supposed x_2 family set	$ b $	33	0.403	0.313	
1. foreside x_1 family set	K_{H-K}	17	5.267	0.973	0.10 for set 1 and set 2
2. backside x_2 family set	K_{H-K}	15	6.000	1.390	0.29 for set 2 and set 3
3. foreside x_2 family set	K_{H-K}	18	5.559	0.842	0.22 for set 1 and set 4
4. backside x_1 family set	K_{H-K}	10	5.772	1.015	

Fig. 9. a. Spectra of the SiO $J = 1-0$ $v = 1$ and 2 lines for the detected sources. The first 8 digit of the 2MASS name and the observing date (yymmdd.d format) are shown.

fig9b.eps

Fig. 9. b. (Continued)

fig9c.eps

Fig. 9. c. (Continued)

fig9d.eps

Fig. 9. d. (Continued)

fig9e.eps

Fig. 9. e. (Continued)

fig9f.eps

Fig. 9. f. (Continued)

fig9g.eps

Fig. 9. g. (Continued)

fig9h.eps

Fig. 9. h. (Continued)

fig9i.eps

Fig. 9. i. (Continued)

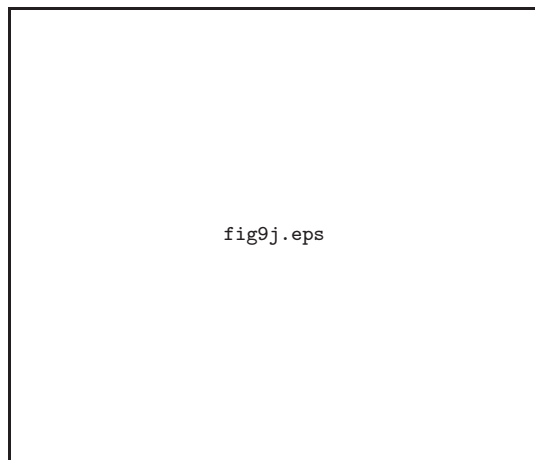


Fig. 9. j. (Continued)